Analytical and Numerical Study of Differential Equation Models for Magnetism

November 9, 2021

Author:
Dimosthenis Vallis

Supervisor:
Stavros Komineas
Vagelis Harmandaris

A thesis submitted in partial fulfillment
of the requirements for the degree of Master of Science
in Applied and Computational Mathematics
with specialization in
Modelling and Analysis in Sciences and Technology

at
the Department of Mathematics & Applied Mathematics
University of Crete

ΠΑΝΕΠΙΣΤΗΜΙΟ ΚΡΗΤΗΣ
UNIVERSITY OF CRETE

Contents

1 Introduction & Approach

In this graduate thesis, we'll present a case by case study of the magnetic fields generated by specific configurations and the Poisson differential equation problem that arises. In the first part, known configurations of analytically solvable magnetizations will be showcased in detail. The general mathematical problem will be constructed. And, it will be attempted to establish the mathematical backbone of such an endeavor and propose some analytical limits. Next, after some *a priori* analysis, we will use various tools to numerically solve cases of finite sources. Finally, particular results will be presented, deduced only through the topology of the magnetization.

Apart from mathematics, numerical simulations of magnetic sources are useful in many other fields. They are especially valuable in material science, where problems with non-trivial magnetic configurations are common. Further, the inspiration for this thesis, the *MagMASim*[1] project, is trying to measure the magnetic fields of celestial bodies using only experimental data. This is a problem of fundamental importance in astrophysics. The Galactic magnetic field affects a wide range of high-interest areas of active research, including: star formation, the astrophysics of the highest-energy particles, and studies of the first moments of the universe.

1.1 The magnetic model

To begin the analysis, a basic inspection of the magnetic material properties is needed. Looking inside matter at an atomic level, there exist microscopic loops of current, charges, electrons rotating and revolving. Those loops are so small that they can be treated as magnetic dipoles. Most materials have a random orientation of atoms, resulting in their interactions to cancel each other, Ref.[30]. But, if a strong enough magnetic field interacts with this material, it can align its dipoles and make it magnetized. The state of magnetic polarization of the material is called *Magnetization* and it is defined as the vector

$$\mathbf{M} \equiv \text{magnetic dipole moment per unit volume,} \tag{1}$$

where magnetic moment is the magnetic strength and orientation of a magnetic dipole. Assuming there are no electric dipoles inside, the effects of this magnetization is to establish bound currents in the material. Those are, a bound volume current density

$$\mathbf{J}_b = \nabla \times \mathbf{M} \tag{2}$$

and a bound surface current density

$$\mathbf{K}_b = \mathbf{M} \cdot \hat{\mathbf{n}} \tag{3}$$

were $\hat{\mathbf{n}}$ is the unit normal vector of the surface, pointing outside. Resulting in the total current density being

$$\mathbf{J} = \nabla \times \mathbf{M} + \mathbf{J}_f \tag{4}$$

where $\mathbf{J}_f$ are the free currents. The magnetic fields generated by the magnetization, inside and outside the material are described by *Maxwell's equations* and the magnetostatic boundary conditions. Later, a couple of useful laws will be used, but all of them are derived from *Maxwell's equations*, Ref.[2].

[1] *Reconstructing the Magnetic field of the Milky way via Astrophysical Techniques and Numerical Simulation.*

$$\begin{aligned} \nabla \cdot \mathbf{B} &= 0 \qquad & \nabla \cdot \mathbf{H} &= -\nabla \cdot \mathbf{M} \\ \nabla \times \mathbf{B} &= \mathbf{J} \qquad & \nabla \times \mathbf{H} &= \mathbf{J}_f \end{aligned} \tag{Maxwell's eq.}$$

where the **H**-field is defined as

$$\mathbf{H} = \frac{1}{\mu_0}\mathbf{B} - \mathbf{M}. \tag{5}$$

Before we try to find those fields, we'll described the tools to achieve it.

1.2 Finite Elements Method & FEniCS

To solve these partial differential equations, in most occasions, numerical solutions are our stronger tool. FEM is used to numerically solve complex differential equation problems. Originally, it was used by engineers for static elastic stress, modal and dynamic analysis, to name a few examples. For instance, they could seek to measure subtle stress changes in the foundation of a bridge, model the torque on metal beams or check if the materials of a rocket will survive the launch. For the above problem, complicated differential equations need to be solved.

Those, of course, were continuous problems and computers can only solve discrete ones. One way to do this, is called Finite Differences. As a derivative is the slope of a function at a point, an approximation can be taken by finding the slope between two points. But, the idea of FEM is quite different from this approach.

At the start of the twentieth century, *B. Galerkin* and others, brought the idea that a combination of some predetermined *trial functions* could get close to the solution. The problem that emerged was how much of each function goes to make the approximation better. *B. Galerkin* worked with two or three functions and he had to be very precise at choosing the best *trial functions*, Ref.[24].

Many years later, as the computer was getting more powerful, those *trial functions* could be hundreds of thousands. And now, the problem to find the coefficients can become a variational problem, with all the known tools available for solving them. Hence, the Finite Elements methods are a combination of this idea with *trial functions* but using many of them. They can be simple functions, like *hat function*, so the interactions are not very complex. Instead of having a differential equation, there is a large system of equations. The unknowns being the coefficients, i.e. *"how much"*, of each *trial function*, Ref.[16].

Nowadays, FEM code has thousands of lines and many companies specialise their code for specific problems. However, FEM was originally created for problems with small changes or variation. For example, in civil engineering, the stress in a material, usually changes slightly and gradually. But now, take fluid mechanics, that always have a flow. Or problems where the gradient of the solution is very high, like a field close to a proton or a source. For such cases, new FEM is needed and there is much work to be done.

In some following chapters, differential equations will be solved using FEM. The *FEniCS Project*[2] is a collection of open-source software components that enables automated solution of differential equations. For our purposes, it is a computing platform that enables us to quickly translate scientific models into finite element Python code. For this study, all models are solved using Lagrange elements. But this can be easily changed for other purposes. As

[2] *FEniCS Project* `https://fenicsproject.org/`, Ref.[34],[35].

mentioned above, the solution is approximated by the sum of the *test functions* times their coefficients,

$$u^{(N)}(\mathbf{x}) = \sum_{i=1}^{N} c_i f_i(\mathbf{x}) \tag{6}$$

where $f(\mathbf{x}_i)$ are the prescribed *test functions*, N is their number and c_i, $i = 0, ..., N$ are the unknown coefficients to be determined. By Lagrange elements is implied that $f(\mathbf{x}_i)$ are Lagrange polynomials and depending on the situation, their degree can be chosen. If a mesh is defined, then it's only needed to assign the values at the boundary of this mesh and let *FEniCS* run the FEM.

1.3 Meshing & Monte Carlo Integration

It is expected that a different mesh is needed for each case. A mesh is defined as a way to divide the space upon which the problem is set. More explicitly, this space is divided in elements that are connected together at nodes. Also known as discretization of the space. This collection of nodes and elements is called the mesh. For 2-dimensional meshes, there are surface elements, like triangular or quadrilateral shaped ones. For our circumstances, although the configurations have specified symmetries, all of them are in three dimensions. Typically, a 3D solid element can be a tetrahedron or hexahedron.

There is a need for freedom to manipulate the density of the mesh. That's because there are specific places of the domain that have high variability. Meanwhile, we don't want to exceed the memory of the hardware by making an extremely dense mesh everywhere. *FEniCS* has tools for creating simple meshes. Instead, we will use *Gmsh* [3], an open source 3D finite element mesh generator. A fast and light meshing tool with parametric input and advanced visualization capabilities. With that said, a way to approximate the values of the

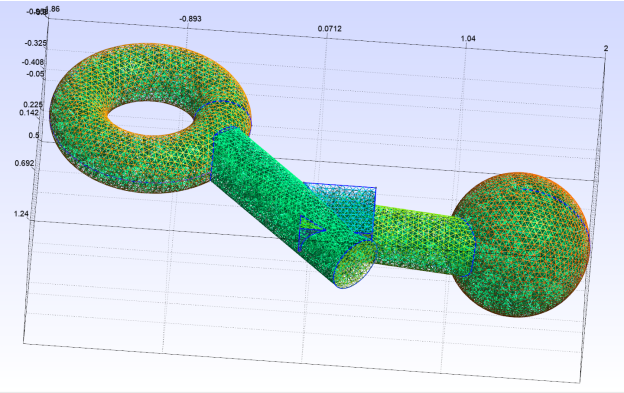

Figure 1: Gmsh interface presenting a "handmade" asymmetric configuration

field in the boundaries is still missing. Later, it will be explained that usually, it's needed to approximate a big complicated integral for each boundary node. In most situations, this can not be solved analytically.

There are several tools for numerical integration. We choose to use *Monte Carlo(MC)* integration. Similar to the midpoint Riemann sum or the trapezoidal rule, we could divide the space in equal parts. Then, as N is getting larger, our approximation will get better.

[3] *Gmsh* `https://gmsh.info/`, Ref.[33].

In the plain MC method, those points are, usually, randomly selected from the uniform distribution, $\mathcal{U}[a,b]$. For the former discretization division, the error will be proportional to $\propto 1/N$ for the simplest methods, like the midpoint Riemann sum. For example, for the trapezoidal rule, it is $\propto 1/N^2$. But for d-dimensional integrals, it becomes $\propto 1/N^{1/d}$ and $\propto 1/N^{2/d}$, accordingly. The error for MC, on the other hand, is $\propto 1/\sqrt{N}$ for every dimension d. Also, its expected that multiple approximations eventually follow a Gaussian distribution. The distribution's mean value approaches the actual solution and attains smaller and smaller variance, as $N \to \infty$. The above are due to the *central limit theorem*.

MC integration is a, relatively, easy method, numerically. It mainly uses the idea of the *law of the large numbers* and *sampling methods*. The expected value $< f >$ of a function over a range $[a,b]$ is

$$< f >= \int_a^b h(\bar{x}) f(\bar{x}) d\bar{x} \Rightarrow \ < f >= \frac{1}{b-a} \int_a^b f(\bar{x}) d\bar{x} \Rightarrow \int_a^b f(\bar{x}) d\bar{x} = (b-a) < f > \quad (7)$$

where the random variable $\bar{x} \sim h(\cdot)$ and h is assumed to be the uniform $\mathcal{U}[a,b]$. Approximating the expected value using N $\{x_i\}$-points with $\{i = 1, 2, ...N\}$, utilising the above-mentioned *law of the large numbers*, the following is derived

$$\int_a^b f(x) dx \approx (b-a) \frac{1}{N} \sum_{i=1}^{N} f(x_i). \quad (8)$$

Note that the function f depends only on one variable but the above can be generalised to any number of variables Ref.([26]).

Creating a sample from a distribution is a whole field in itself. Pseudo-random numbers are generated with linear congruent methods, special algorithms like *the Mersenne Twister* or even using samples from the noise of the atmosphere. For this thesis, we exploit the generators of *scipy* library in *Python* that indeed use *the Mersenne Twister*, Ref.([38]).

Finally, MC integration remains consistent in higher dimensions. Additionally, it is much less cumbersome for the hardware, considering the thousands of boundary node integrals that have to be solved.

2 Cases with analytical solutions

Before the numerical problems are computed, we present an approach to solve some of the most basic configurations. Some are finite sources like the ones in Chapter (2.1). Some other are considered as infinite sources. Those are modeling the case of the field very close to a source. What they have in common is a very specific symmetry. Thus, we can avoid solving differential equations to find the produced field.

2.1 Point dipole and magnetized sphere

It's useful to visualise the fields of some specific sources that appear in nature. Apart from matter, a star or star cluster, if it has fixed magnetization, is similar to a point dipole or a spherical source to the viewer who is far way.

Implementing the Biot-Savard law of magnetostatics, the magnetic field $\mathbf{B}(\mathbf{r})$ produced in a point space $\mathbf{r} = (x, y, z)$ by a distribution of steady currents in a volume V' is

$$\mathbf{B}(\mathbf{r}) = \frac{\mu_0}{4\pi} \int_{V'} \frac{\mathbf{j}(\mathbf{r}') \times (\mathbf{r} - \mathbf{r}')}{|\mathbf{r} - \mathbf{r}'|^3} \, dV'. \tag{9}$$

In equation (9), μ_0 is the permeability of vacuum, $\mathbf{j}(\mathbf{r}')$ is the current density in a point $\mathbf{r}' = (x', y', z')$ of the magnetic source, and the integration is performed over the whole distribution of currents.

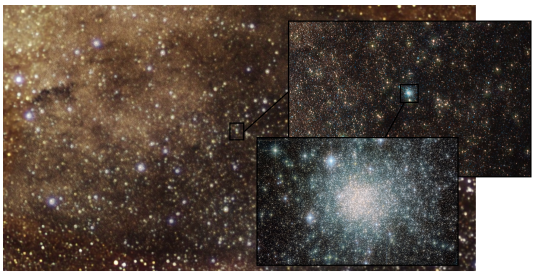

Figure 2: Star cluster Terzan 5 taken with Hubble, the Very Large Telescope at ESO's Paranal Observatory and the Keck Telescope

Using

$$\frac{\mathbf{r} - \mathbf{r}'}{|\mathbf{r} - \mathbf{r}'|^3} = -\nabla \left(\frac{1}{|\mathbf{r} - \mathbf{r}'|} \right)$$

and substituting in Eq.(9)

$$\mathbf{B}(\mathbf{r}) = \frac{\mu_0}{4\pi} \nabla \times \int_{V'} \frac{\mathbf{j}(\mathbf{r}')}{|\mathbf{r} - \mathbf{r}'|} \, dV' \Rightarrow \nabla \times \mathbf{A}(\mathbf{r}) = \frac{\mu_0}{4\pi} \nabla \times \int_{V'} \frac{\mathbf{j}(\mathbf{r}')}{|\mathbf{r} - \mathbf{r}'|} \, dV' \tag{10}$$

$$\Rightarrow \mathbf{A}(\mathbf{r}) = \frac{\mu_0}{4\pi} \int_{V'} \frac{\mathbf{j}(\mathbf{r}')}{|\mathbf{r} - \mathbf{r}'|} \, dV' + \nabla\psi. \tag{11}$$

The gradient of an arbitrary scalar function ψ implies that for a magnetic induction, the potential $\mathbf{A}$ can be freely transformed according to the *Gauge Transformation*

$$A \to A + \nabla.$$

Assuming there are no sources at infinity its allowed to use (Ref.[1])

$$\mathbf{A}(\mathbf{r}) = \frac{\mu_0}{4\pi} \int_{V'} \frac{\mathbf{j}(\mathbf{r}')}{|\mathbf{r} - \mathbf{r}'|} \, dV'. \tag{12}$$

Equation (12) can be expanded in powers of r^{-1} through the *multipole expansion.*

$$\mathbf{A}(\mathbf{r}) = \frac{\mu_0}{4\pi} \sum_{n=0}^{\infty} \frac{1}{r^{n+1}} \int_{V'} (r')^n \mathbf{j}(\mathbf{r}') P_n(\cos\alpha) \, dV' \tag{13}$$

where P_n are the Legendre polynomials and α is the angle between r and r'. For $n = 0$

$$\mathbf{A_m}(\mathbf{r}) = \frac{\mu_0}{4\pi \mathbf{r}} \int_{V'} \mathbf{j}(\mathbf{r}') \, dV'. \tag{14}$$

This is the vector potential of the magnetic monopole and it is shown to vanish, Ref.[8].

Continuing, for $n = 1$,

$$\mathbf{A_d}(\mathbf{r}) = \frac{\mu_0}{4\pi} \frac{1}{r^3} \int_{V'} (\mathbf{r} \cdot \mathbf{r}') \mathbf{j}(\mathbf{r}') \, dV' \tag{15}$$

Then, if

$$\mathbf{m} = \frac{1}{2} \int_{V'} \mathbf{r} \times \mathbf{j}(\mathbf{r}') \, dV'.$$

is the magnetic (dipole) moment, the vector potential can be put in the following form

$$\mathbf{A_d}(\mathbf{r}) = -\frac{\mu_0}{4\pi}\mathbf{m} \times \nabla\frac{1}{r}. \tag{16}$$

Keeping in mind that $\mathbf{m}$ is a fixed vector and applying the product rule, the magnetic field produced by a single dipole is

$$\mathbf{B_d}(\mathbf{r}) = \frac{\mu_0}{4\pi}\frac{3(\mathbf{m}\cdot\mathbf{r})\mathbf{r} - r^2\mathbf{m}}{r^5}. \tag{17}$$

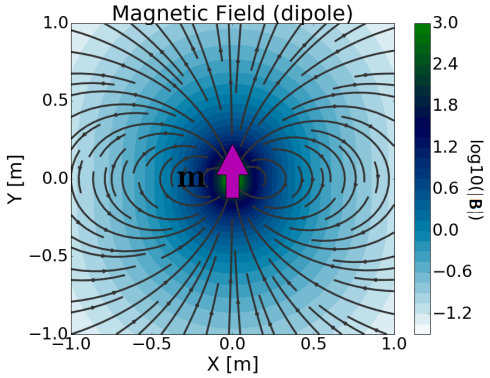

Figure 3: Field lines visualized in 3D space of a magnetic field generated by Magnetic Dipole of $\mathbf{m} = 1Am^2$. Ref.[8].

We put the origin at the dipole and the z-axis oriented as $\mathbf{m}$. This way, there is a rotational symmetry, meaning the field is invariant on rotations around Oz. In that configuration, the most appropriate coordinate system is cylindrical (ρ, ϕ, z) and the corresponding unit vectors $(\hat{\mathbf{e}}_\rho, \hat{\mathbf{e}}_\phi, \hat{\mathbf{e}}_z)$. Thus, equation (16) becomes

$$\mathbf{A_d}(\mathbf{r}) = -\frac{\mu_0}{4\pi}(m\hat{\mathbf{e}}_z) \times (-\frac{1}{r^2}\hat{\mathbf{e}}_r) \Rightarrow \mathbf{A_d}(\mathbf{r}) = -\frac{\mu_0}{4\pi}(m\hat{\mathbf{e}}_z) \times [-\frac{1}{r^2}(\sin\theta\hat{\mathbf{e}}_\rho + \cos\theta\hat{\mathbf{e}}_z)]$$

$$\Rightarrow \mathbf{A_d}(\mathbf{r}) = -\frac{\mu_0}{4\pi}(m\hat{\mathbf{e}}_z) \times (-\frac{1}{r^2}\sin\theta\hat{\mathbf{e}}_\rho)$$

$$\Rightarrow \mathbf{A_d}(\mathbf{r}) = \frac{\mu_0}{4\pi}\frac{m}{r^2}\sin\theta\ \ \hat{\mathbf{e}}_\phi \tag{18}$$

and the formula for the magnetic field becomes

$$\mathbf{B_d}(\mathbf{r}) = \frac{\mu_0}{4\pi r^5}[3(mr\cos\theta)r\ \ \hat{\mathbf{e}}_r - r^2 m\ \ \hat{\mathbf{e}}_z] \Rightarrow \mathbf{B_d}(\mathbf{r}) = \frac{\mu_0}{4\pi r^5}\Big[3mr^2[\cos\theta\ \ (\sin\theta\hat{\mathbf{e}}_\rho + \cos\theta\hat{\mathbf{e}}_z)] - r^2 m\ \ \hat{\mathbf{e}}_z\Big]$$

$$\Rightarrow \mathbf{B_d}(\mathbf{r}) = \frac{\mu_0}{4\pi}\frac{m}{r^3}\Big[\frac{3}{2}\sin(2\theta)\ \ \hat{\mathbf{e}}_\rho + (3\cos^2\theta - 1)\hat{\mathbf{e}}_z\Big]. \tag{19}$$

The validity of proposed numerical methods can now be tested. The above solution of Eq.(19) can be used to find the Dirichlet boundary condition for a Laplace's equation on a spherical boundary. In Chapters (3) and (4), a more elaborate explanation will be given for such a numerical problem construction and for the methodology used.

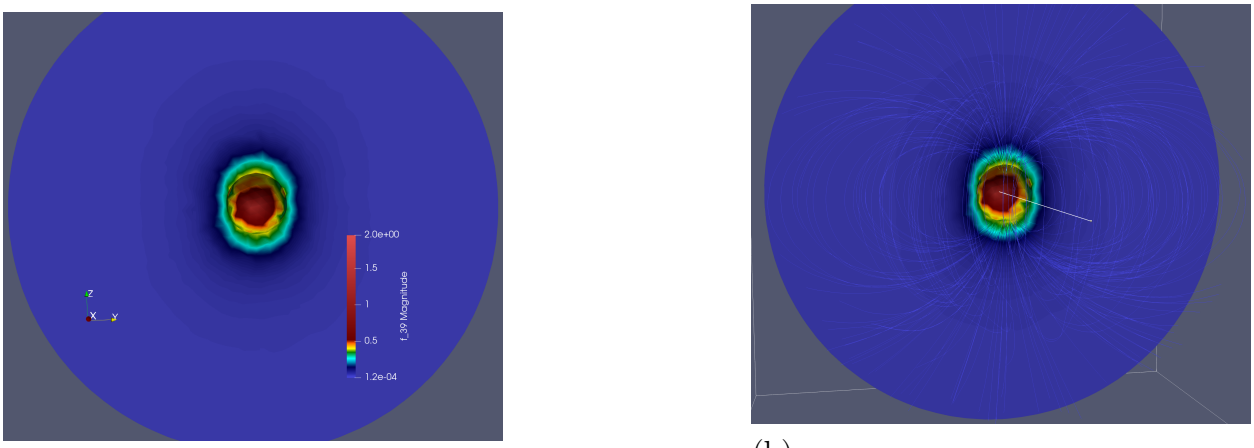

(a) Magnitude of field on z-y pane

(b) Field lines visualized in 3D space of Magnetic field

Figure 4: Values of the B magnetic field generated by dipole magnetization of unit magnitude derived through a Laplace boundary value problem(BVP). It was approximated in a mesh of 8941 nodes, 2191 of which were on the boundary of the domain.

The tool used to visualise all the vector fields from now on is *Paraview*[4].

At a first glance, the field lines seem to make sense. Now, the known solution can be taken advantage to evaluate errors in FEM. Using the L^2-norm to get the errors, Fig.(5) is produced. This can be considered as a proof of concept and proceed, in Chapter (4), to use

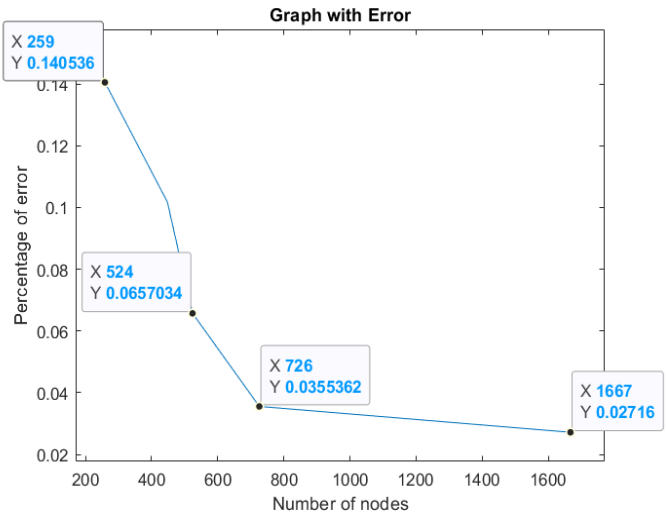

Figure 5: Plot line showing the logarithmic decline of the values of error for different number of nodes for the dipole configuration in Fig.(4).

the method for configurations without analytical solutions.

Let's now begin to find the magnetic field of a uniformly magnetised sphere.
Let a sphere of radius R be uniformly magnetised with magnetic moment $\mathbf{m} = \frac{4}{3}\pi R^3 \mathbf{M}$ with $\mathbf{M}$ the uniform magnetization vector. A basic model of this sphere is a group of elementary point dipoles.

[4] *Paraview* `https://www.paraview.org/python/`

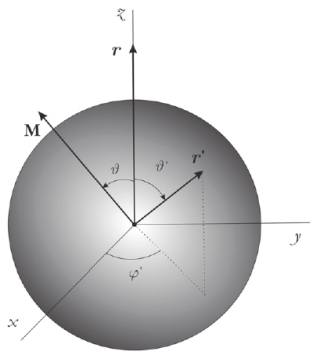

Figure 6: Uniformly magnetized sphere and paramertization of the point measured as (r, θ, ϕ). Also, of points of the source as (r', θ', ϕ').

The potential by this sphere at point $\mathbf{r}$ is the sum of the contributions of all the volumes dV' at distance r' and elementary dipole moment $d\mathbf{m} = \mathbf{M}dV'$.
So, (12) becomes

$$\mathbf{A_d}(\mathbf{r}) = -\frac{\mu_0}{4\pi}\int_{V'} \mathbf{M} \times \nabla' \frac{1}{|r - r'|}\, dV'. \tag{20}$$

And considering $\mathbf{M}$ is uniform,

$$\mathbf{A_d}(\mathbf{r}) = -\frac{\mu_0}{4\pi}\int_{V'} \nabla' \times \frac{\mathbf{M}}{|r - r'|}\, dV' \tag{21}$$

the sphere as a domain is smooth, Stokes' Theorem can be applied. So the integral will now be over the surface S' of the sphere

$$\mathbf{A_d}(\mathbf{r}) = \frac{\mu_0}{4\pi}\oint_{S'} \frac{\mathbf{M} \times \mathbf{n}}{|r - r'|}\, dS' \tag{22}$$

with $\mathbf{n} = \mathbf{r}'/r'$ the unit vector normal to S' and with surface parameterization
$dS' = R^2\theta' d\theta' d\phi'$. From here on, it's only a matter of choosing the right coordinate system and orientation to simplify the answer as much as possible. Now, the space origin is put at the center of the sphere and the z-axis on $\mathbf{r} = r\hat{\mathbf{e}}_z$. Also, from Figure (6)

$$\mathbf{r}' = R(\sin\theta'\cos\phi', \sin\theta'\sin\phi', \cos\theta') \tag{23}$$

and

$$|\mathbf{r} - \mathbf{r}'| = (r^2 + R^2 - 2rR\ \cos\theta')^{1/2}. \tag{24}$$

WLOG $\mathbf{M}$ can be thought of as forming an angle θ with $\mathbf{r}$ confined in the $x - y$ plane, meaning $\mathbf{M} = M(\sin\theta, 0, \cos\theta)$ and

$$\mathbf{M} \times \mathbf{n} = M(-\sin\phi'\sin\theta'\cos\theta, \sin\theta'\cos\phi'\cos\theta - \cos\theta'\sin\theta, \sin\theta'\sin\phi'\sin\theta).$$

Making these substitutions on (22), note that all the contributions of ϕ' disappear if we integrate over [0,2π). The rest of the terms give

$$\mathbf{A_d}(\mathbf{r}) = \begin{cases} \dfrac{\mu_0}{4\pi}\dfrac{mr}{R^3}\sin\theta\hat{\mathbf{e}}_\phi & , r \le R \\ \\ \dfrac{\mu_0}{4\pi}\dfrac{m}{r^2}\sin\theta\hat{\mathbf{e}}_\phi & , r > R \end{cases}. \tag{25}$$

Taking the curl inside and outside the ball respectively, it follows

$$\mathbf{B_d}(\mathbf{r}) = \begin{cases} \frac{\mu_0}{4\pi}\frac{m}{R^3}\hat{\mathbf{e}}_z & , r \leq R \\ \\ \frac{\mu_0}{4\pi}\frac{m}{r^2}\left[\frac{3}{2}\sin(2\theta)\hat{\mathbf{e}}_\rho + (3\cos^2\theta - 1)\hat{\mathbf{e}}_z\right] & , r > R \end{cases}. \tag{26}$$

The above are some rare cases that the field of finite sources can be procured analytically. Continuing with Chapter (2), we'll tackle some infinite sources.

2.2 Infinite Sources

A long circular cylinder of radius R has a "frozen-in" uniform Magnetization $\mathbf{M}$ parallel to the axis. We will use cylindrical coordinates (ρ, ϕ, z) and the corresponding unit vectors $(\hat{\mathbf{e}}_\rho, \hat{\mathbf{e}}_\phi, \hat{\mathbf{e}}_z)$. Applying Ampère's law for $\mathbf{H} = \frac{1}{\mu_0}\mathbf{B} - \mathbf{M}$, any loop we choose, won't have any free currents enclosed. There are only bounded currents, since the magnetization of the cylinder is uniform. We derive from the volume bound currents

$$\mathbf{J}_b = \nabla \times \mathbf{M} = \mathbf{0}. \tag{27}$$

But we have surface currents

$$\mathbf{K}_b = \mathbf{M} \times \mathbf{n} = M\hat{\mathbf{e}}_z \times \hat{\mathbf{e}}_\rho \Rightarrow \mathbf{K}_b = M\hat{\mathbf{e}}_\phi. \tag{28}$$

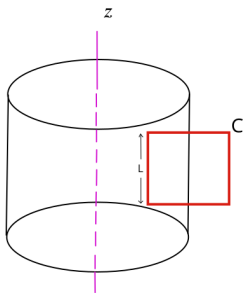

Figure 7: Ampèrian loop(red) of side length L, that's half inside and half outside from a part of an infinite cylinder(black) oriented on the z-axis.

Choosing a loop (C) of length L and since $\mathbf{H}$ points in the axial direction, we have

$$\oint_C \mathbf{H}\cdot\mathbf{dl} = 0 \Rightarrow \mathbf{H}L = 0 \Rightarrow \mathbf{H} = \mathbf{0} \Rightarrow \frac{\mathbf{B}}{\mu_0} - \mathbf{M} = \mathbf{0} \Rightarrow \mathbf{B} = \mu_0\mathbf{M} = \mu_0 M\hat{\mathbf{e}}_z \tag{29}$$

$$\Rightarrow \mathbf{B} = \begin{cases} \mu_0 M\hat{\mathbf{e}}_z & , \rho \leq R \\ \\ 0 & , \rho > R \end{cases} \tag{30}$$

since there's no magnetization outside the cylinder.
We can even use the boundary conditions of Maxwell's equations for $\mathbf{H}$, to verify

$$H^\perp_{out} - H^\perp_{in} = -(M^\perp_{out} - M^\perp_{in}) \Rightarrow H^\perp_{out} - \cancelto{0}{H^\perp_{in}} = -(\cancelto{0}{M^\perp_{out}} - \cancelto{0}{M^\perp_{in}}) \Rightarrow H^\perp_{out} = 0 \tag{31}$$

$$\mathbf{H}^{\parallel}_{out} - \mathbf{H}^{\parallel}_{in} = \mathbf{K}_f \times \mathbf{n}_s \Rightarrow \mathbf{H}^{\parallel}_{out} - \mathbf{H}^{\parallel}_{in} = \cancelto{0}{\mathbf{K}_f \times \mathbf{n}_s} \Rightarrow \mathbf{H}^{\parallel}_{out} = \cancelto{0}{\mathbf{H}^{\parallel}_{in}} \Rightarrow \mathbf{H}^{\parallel}_{out} = 0. \tag{32}$$

The above directional indexes refer to the parallelity and perpendicularity with the surface of the cylinder. Also, $\mathbf{K}_f$ is the free surface current which is 0 and $\mathbf{n}_s$ is the surface normal.

For a magnetized infinite slab with thickness b and a perpendicular, uniform magnetization, a different argument has to be applied. We can assume infinite small loops of current that form around the magnetization lines. Such a model is the definition of $\mathbf{M}$ as described at the start of Chapter (2). It can be assumed that those loops are the ones that create the magnetic field $\mathbf{B}$, but it is easy to see that all the loops eventually cancel each other, even in the borders of the slab. So, $\mathbf{B} = 0$ and $\mathbf{H} = -\mathbf{M}$ inside the slab.

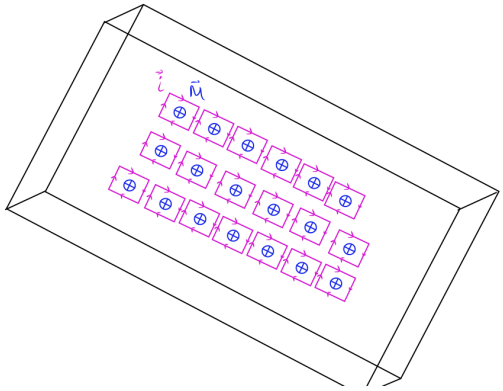

Figure 8: Homogeneous magnetization(blue) oriented perpendicular to the slab and generated by very small current loops(pink). The loops are shown to cancel each other at every point of the infinite slab.

From the above, inside the slab

$$\mathbf{B} = 0 \quad , -\frac{b}{2} < z < \frac{b}{2}. \tag{33}$$

But to get the field outside we will again use the boundary conditions.

$$H^{\perp}_{out} - H^{\perp}_{in} = -(M^{\perp}_{out} - M^{\perp}_{in}) \Rightarrow H^{\perp}_{out} - H^{\perp}_{in} = -(\cancelto{0}{M^{\perp}_{out}} - M^{\perp}_{in}) \Rightarrow H^{\perp}_{out} = M^{\perp}_{in} + H^{\perp}_{in}$$

$$\Rightarrow H^{\perp}_{out} = M^{\perp}_{in} - M^{\perp}_{in} \Rightarrow H^{\perp}_{out} = 0 \tag{34}$$

$$\mathbf{H}^{\parallel}_{out} - \mathbf{H}^{\parallel}_{in} = \mathbf{K}_f \times \mathbf{n}_s \Rightarrow \mathbf{H}^{\parallel}_{out} - \mathbf{H}^{\parallel}_{in} = \cancelto{0}{\mathbf{K}_f \times \mathbf{n}_s} \Rightarrow \mathbf{H}^{\parallel}_{out} = \mathbf{H}^{\parallel}_{in}$$

$$\Rightarrow \mathbf{H}^{\parallel}_{out} = \cancelto{0}{\mathbf{M}^{\parallel}_{in}} \Rightarrow \mathbf{H}^{\parallel}_{out} = 0. \tag{35}$$

Or we could use the same argument as with the cylinder and the Ampèrian loop and determine that $\mathbf{H} = 0$ outside the slab shown in Fig.(9). So finally,

$$\mathbf{B} = 0 \quad , z \in \mathbb{R}.$$

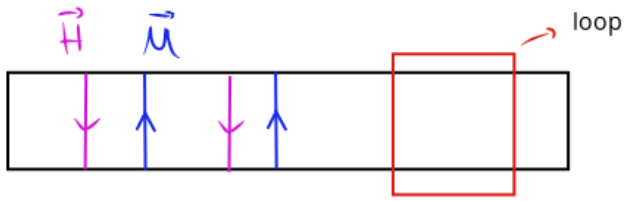

Figure 9: Ampèrian loop(red) in magnetized slab of thickness b, the magnetization(blue) and the H-field(pink) are shown to cancel each other at every point of the slab contributing to $\mathbf{B} = 0$

.

Remark. The same conclusion regarding the disappearance of particular fields outside the magnet can be gained by the $\mathbf{M} \times \mathbf{n}$ term of equation (22).

3 Problem Construction

In general, the time-independent magnetization produces a magnetic field according to Maxwell's equations, as such:

$$\begin{aligned} \nabla \cdot \mathbf{H} &= -\nabla \cdot \mathbf{M} \\ \nabla \times \mathbf{H} &= 0. \end{aligned} \tag{36}$$

We choose to deal with the H-field(or magnetic field) because it can safely be assumed that its curl is zero. Additionally, it's always found by solving a Poisson equation, as shown later. We'll sometimes end the analysis when finding the H-field since the usual $\mathbf{B}$, magnetic flux density, can be calculated plainly by Eq.(37).

$$\mathbf{B} = \mu_0(\mathbf{H} + \mathbf{M}) \tag{37}$$

where μ_0 is the vacuum permeability. We are usually bothered with the field outside the source, so μ_0 becomes only a scaling factor. It is not certain that the equation has a solution for all domains, though.

We define the magnetostatic potential ψ as

$$\mathbf{H} = -\nabla\psi. \tag{38}$$

From that we derive a Poisson equation

$$\nabla \cdot \mathbf{H} = -\nabla \cdot \mathbf{M} \Rightarrow \nabla \cdot (-\nabla\psi) = -\nabla \cdot \mathbf{M} \Rightarrow \Delta\psi = \nabla \cdot \mathbf{M}. \tag{39}$$

Its formal solution is

$$\psi = -\int_V \frac{\nabla \cdot \mathbf{M}(\mathbf{r}')}{|\mathbf{r} - \mathbf{r}'|} dV' + \oint_S \frac{\mathbf{M}(\mathbf{r}') \cdot \mathbf{dS}'}{|\mathbf{r} - \mathbf{r}'|}. \tag{40}$$

where V is the volume of the material (where $M \neq 0$) and S is the surface of volume V .

3.1 Domain analysis

There's a need to be careful with the above analysis as some, deceptively strong, arguments don't hold under all domains. We'll choose to comment on the configuration of a cone-like domain. It can't be supposed that even the derivatives exist in the apex and the directrix of the cone. Then the argument will expand to suggest which types of domains have meaning for the Laplace problem.

Lemma 1. On a convex polyhedral domain, an irrotational and divergence-free vector field is described by a Laplace equation of a scalar field.

Proof. Let's assume our cone to be the linear image of a convex polyhedron. This is indeed safe to assume, since the data we will have on the boundary is not continuous. This also true, for values gained from numerical integration or from experiment.

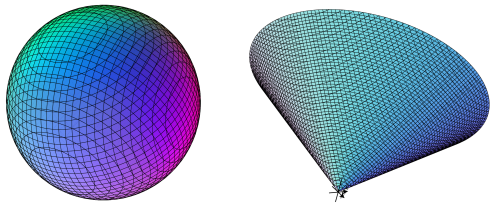

Figure 10: Visualizing the linear transformation from a polyhedral "sphere"(left) that is convex domain, to the polyhedral "cone"(right).

The stability of Helmholtz decomposition in 3 dimensions is known to hold for convex polyhedral regions, Ref.[14]. A cone, for $z \geq 0$, is, of course, a usual example of a convex domain. The decomposition can be used to write the $\mathbf{F}(\mathbf{x})$ as the sum of an irrotational (curl-free) vector field and a solenoidal (divergence-free) vector field. In other words, it can be separated as a sum of the gradient of a scalar potential and a curl of a vector potential.

$$\mathbf{F}(\mathbf{x}) = -\nabla\psi + \nabla \times \mathbf{A}.$$

Assuming $\mathbf{F}(\mathbf{x})$ is an irrotational field.

$$\nabla \times \mathbf{F}(\mathbf{x}) = 0 \Rightarrow \nabla \times (-\nabla\psi + \nabla \times \mathbf{A}) = 0 \Rightarrow \nabla \times \nabla \times \mathbf{A} = 0 \Rightarrow \nabla \times \mathbf{A} = \nabla\psi'$$

due to the fact that $\nabla \times \mathbf{A}$ is divergence free by definition

$$\nabla \times \mathbf{A} = 0.$$

The decomposition becomes

$$\mathbf{F}(\mathbf{x}) = -\nabla\psi.$$

Also, defining $\mathbf{F}(\mathbf{x})$ as a divergence-free vector field:

$$\begin{cases} \nabla \times \mathbf{F}(\mathbf{x}) = \mathbf{0} \\ \nabla \cdot \mathbf{F}(\mathbf{x}) = 0 \end{cases} \Rightarrow \begin{cases} \mathbf{F}(\mathbf{x}) = -\nabla\psi \\ \nabla \cdot \mathbf{F}(\mathbf{x}) = 0 \end{cases}$$

$$\Rightarrow \nabla \cdot (-\nabla\psi) = 0 \Rightarrow -\Delta\psi(\mathbf{x}) = 0. \qquad \text{(Laplace's equation)}$$

■

Remark. The domain cannot have point discontinuities, not inside nor in the boundaries, because, even if a Laplace equation can be solved in such a domain, Helmholtz theorem does not hold, so this was not Laplace problem in the first place, Ref.[19].

3.2 Existence and Uniqueness

It's, of course, very important to know if such a problem has a solution and what are the conditions of such property. Thanks to the works of *Schwarch*(1870), *Neummann*(1877), *Hilbert*(1899) and many others, it's proven that the Dirichlet case

$$\begin{aligned} \Delta u &= 0, \quad \Omega \\ u &= g, \quad \partial\Omega \end{aligned} \tag{BVP}$$

with $\Omega \subset \mathbb{R}^3$ a bounded domain and $g : \partial\Omega \to \mathbb{R}$ bounded and continuous on the boundary, has a solution. As usual, $\Omega = \overline{\Omega} - \partial\Omega$.
Now, it's only a matter of uniqueness.

Theorem (Weak Maximum Principle). As stated in (p.27) in Ref.[7], suppose u is harmonic within Ω. Then

$$\max_{\overline{\Omega}} u = \max_{\partial\Omega} u.$$

A similar theorem exists for the minimum of u.

Lemma 2. For this harmonic Dirichlet problem (BVP), if a solution exists, it is unique.

Proof. (**Uniqueness**)
Suppose both $u_1(\mathbf{x}), u_2(\mathbf{x})$ are solutions of (BVP). Let's, also, define

$$w(\mathbf{x}) = u_1(\mathbf{x}) - u_2(\mathbf{x}), \quad \mathbf{x} \in \overline{\Omega}.$$

Which is, obviously, also a solution considering the Laplace operator is a linear one.

$$\Delta(u_1(\mathbf{x}) - u_2(\mathbf{x})) = \Delta u_1 - \Delta u_2 = 0 - 0 = 0 \Rightarrow \Delta w(\mathbf{x}) = 0, \quad \mathbf{x} \in \Omega.$$

Additionally, about the boundary condition, its appointed that

$$\begin{cases} u_1 = g, & \partial\Omega \\ u_2 = g, & \partial\Omega \end{cases} \Rightarrow u_1 - u_2 = 0 \Rightarrow w(\mathbf{x}) = 0, \quad \mathbf{x} \in \partial\Omega.$$

Substituting in the (BVP), the new Dirichlet problem becomes

$$\begin{aligned} \Delta w &= 0, \quad \Omega \\ w &= 0, \quad \partial\Omega \end{aligned} .$$

Following from the *Weak Maximum Principal* the maximum of w must be taken at the boundary so $w \leq 0$. Similarly, from the *Weak Minimum Principal* follows $w \geq 0$. So,

$$0 \leq w \leq 0 \Rightarrow w(\mathbf{x}) = 0, \quad \mathbf{x} \in \overline{\Omega}.$$

Thus, $u_1 = u_2 = u$ for any u_1, u_2 solutions of (BVP).

■

Remark. We want to remark that there are other ways to get rid of the awkward sub-domains. Either by "smoothing" the apex or creating any domain with at least $C^{1,a}$ continuity. With $C^{k,a}$, the a-Hölder continuity condition, with k the order of the derivative, Ref.[20].

4 Finite Sources - Numerical solutions

For most finite sources, the methods in Chapter (2) can't be used. Let us start with simple cases of magnetization and up the complexity as we go; proceeding to solve the Poisson equation numerically.

The integral of Eq.(40) in the boundaries will always be approximated using MC integration. An approximation of the integrated function will be computed numerically through random sampling, after some analytical manipulation to the integral. The integral can be approximated by averaging samples of the function. The points are sampled from the uniform distribution within the 3D or 2D interval. For the three dimensional case, given a set of $3N$ uniform random variables, the following N random vectors are constructed

$$\mathbf{X}_i = \begin{bmatrix} x_i \in [a_x, b_x] \\ y_i \in [a_y, b_y] \\ z_i \in [a_z, b_z] \end{bmatrix}, i = 1, 2, \ldots, N \tag{41}$$

and the approximation adapted for the 3 dimensions is,

$$\psi^N_{|(x,y,z)=boundary\,point} = \frac{Volume(a_x, b_x, a_y, b_y, a_z, b_z)}{N} \sum_{i=1}^{N} F(x, y, z, x_i^{'}, y_i^{'}, z_i^{'})$$

with $F(\mathbf{r}, \mathbf{r}')$ being the integrand, Ref.[15]. Following the values for all the chosen boundary nodes, the FE method will be applied to find the values on the interior domain. There will be some indicative Python code that does that after the **References** (8).

4.1 Homogeneous case

We start with the simple case of a homogeneous magnetization in a finite cylinder. Meanwhile, we can use this opportunity to check if and how fast our MC method converges to a single value.
Let us assume a magnetization configuration, like so:

$$\mathbf{M} = k\hat{\mathbf{e}}_z. \tag{42}$$

The axis of the cylinder is chosen to be the z-axis. Its height is from $z_a = -1$ to $z_b = 1$ and the radius is $R = 0.5$. All those, clearly, can be changed to suit the user. Evidently, the divergence of $\mathbf{M}$ is zero. And the Laplace equation acquired is

$$\Delta\psi = 0. \tag{43}$$

Only the surface integral contribution of Eq.(40) is needed for the solution of the differential equation, given that $\nabla \cdot \mathbf{M} = 0$.

$$\psi(\rho, z) = \oint_S \frac{\mathbf{M}(\mathbf{r}') \cdot \mathbf{dS}'}{|\mathbf{r} - \mathbf{r}'|}$$

$$\Rightarrow \psi(\rho, z) = \oint_{top\,cap} \frac{\mathbf{M}(\mathbf{r}') \cdot \mathbf{dS}'}{|\mathbf{r} - \mathbf{r}'|} + \oint_{lower\,cap} \frac{\mathbf{M}(\mathbf{r}') \cdot \mathbf{dS}'}{|\mathbf{r} - \mathbf{r}'|} + \oint_{cylinder} \frac{\cancelto{0}{\mathbf{M}(\mathbf{r}') \cdot \mathbf{dS}'}}{|\mathbf{r} - \mathbf{r}'|}$$

$$\Rightarrow \psi(\rho, z) = \int_0^R \int_0^{2\pi} \frac{k\rho' \, d\rho' d\phi'}{(\rho^2 + \rho'^2 - 2\rho\rho' \cos\phi' + (z - z_b)^2)^{1/2}} + \int_0^R \int_0^{2\pi} \frac{k\rho' \, d\rho' d\phi'}{(\rho^2 + \rho'^2 - 2\rho\rho' \cos\phi' + (z - z_a)^2)^{1/2}}. \tag{44}$$

The above formula will be proven in Chapter (4.2). The surface integral will be approximated on a cylindrical boundary, outside the source and near the cylindrical source. Afterwards, these values will be used as boundary condition to solve the Poisson problem numerically.

Making many iterations to determine the value of the field in a single boundary point, we gather enough data to appraise this MC algorithm. It seems safe to deduce that, for this

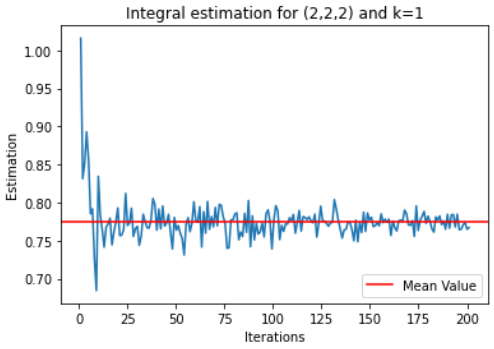

(a) Convergence to a single value after 200 iterations

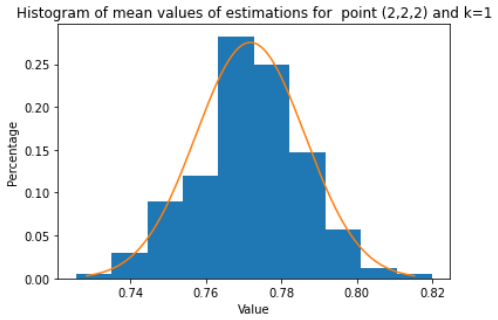

(b) Mean values of 30 different iterations approaching Normal distribution

Figure 11: Plain Monte Carlo integration values of the integral of Eq.(44) on a single point. After multiple approximations the results follow a normal distribution and they converge on a single value after a number of iterations.

configuration, choosing > 100 iterations is a good rule of thump. Nevertheless, this is a case by case particularity. After appointing values on every integral in the boundary, FEM is used to, finally, find the magnetic field inside the chosen volume and near the source. The created mesh has 792 nodes on the boundary and 1432 nodes in total. It has a cylindrical shape and a hole where the source is. The values on Fig.(12) are of the H-field, as the problem is described in Chapter (3). If the area outside the source is assumed to be a perfect vacuum, the usual B-field is just $\mu_0 H$, following Eq.(5). The magnetization outside the source is zero. Notice the expected symmetry in the field lines. Further, there's no need to check the magnitude of the field everywhere to get a picture of what transpires. Given this symmetry, using only the z-y plain (or z-x plain or any rotation of such plain around the z-axis) is enough to demonstrate the data.

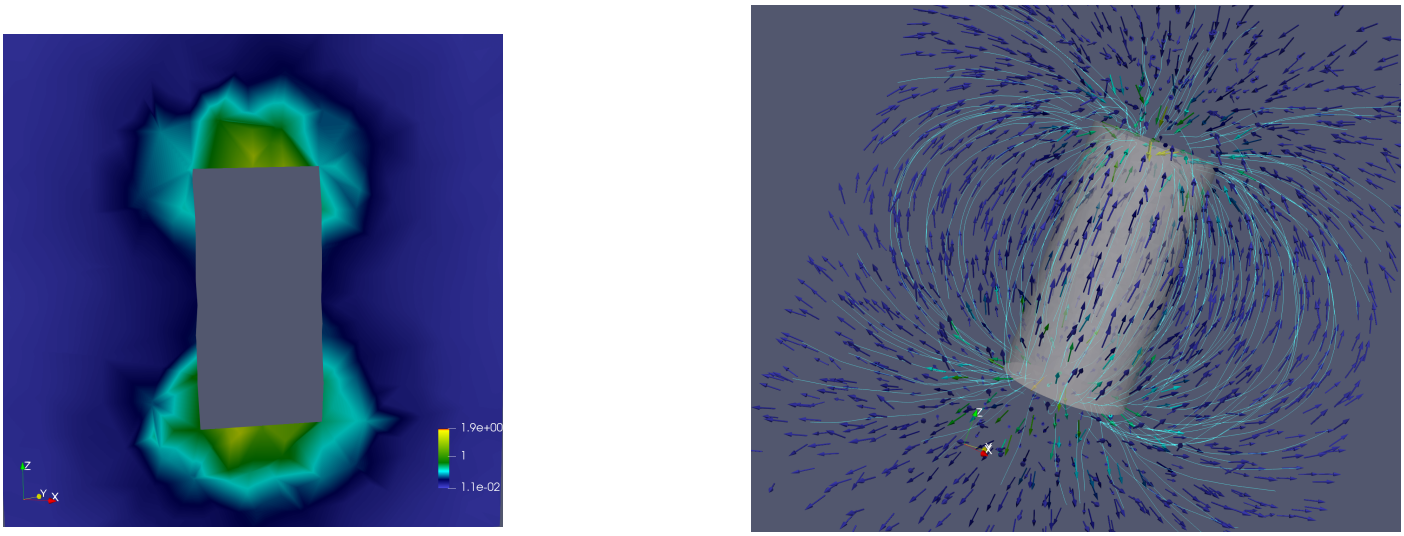

(a) Magnitude of field on z-y pane

(b) Field lines visualized in 3D space of Magnetic field

Figure 12: Values of the H magnetic field generated by homogeneous magnetization of unit magnitude oriented at z-axis derived through a Laplace BVP. It was approximated in a mesh of 1432 nodes, 792 of which were on the boundary of the domain. The approximations of the boundary values were made with 300 MC iterations.

A rather crude way to test the results is finding the integral with MC at all the nodes of the mesh. Then, it can be assessed if the error is decreasing as the iterations go up. This does not mean that the solutions are accurate, it just denotes that they converge on a similar value.

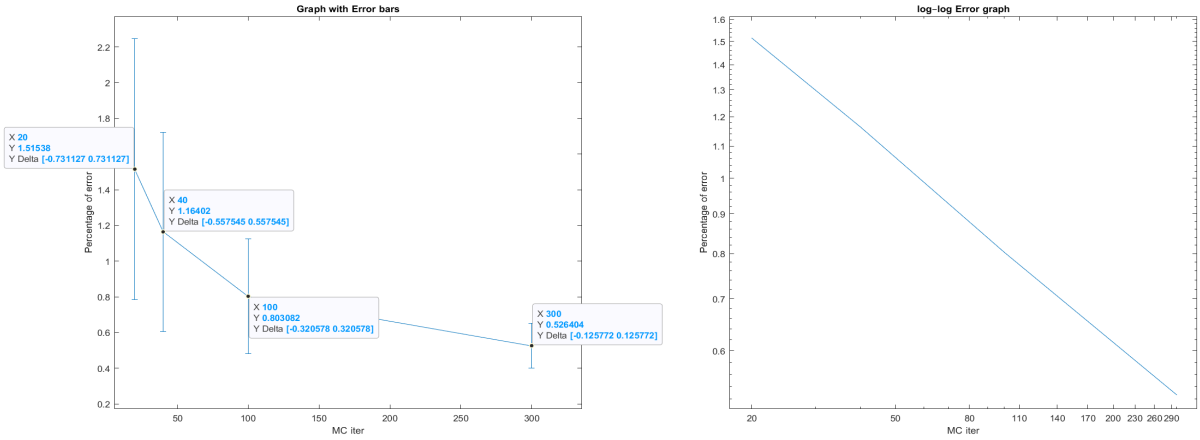

Figure 13: Mean values of error for different MC iterations shown to decrease. Also, the errors' variance is reduced with every step(left). Moreover, its shown that the error decreases as logarithm (right) for 1448 nodes.

These results will be used as a proposal that this method, given a dense enough mesh and high enough MC iterations, will converge.

4.2 Equivariant configuration

Let us assume a magnetization configuration of the form

$$\mathbf{M}(\rho, z) = M_\rho(\rho, z)\hat{\mathbf{e}}_\rho + M_\phi(\rho, z)\hat{\mathbf{e}}_\phi + M_z(\rho, z)\hat{\mathbf{e}}_z \tag{45}$$

where (ρ, ϕ, z) are cylindrical coordinates and $\hat{\mathbf{e}}_\rho, \hat{\mathbf{e}}_\phi, \hat{\mathbf{e}}_z$ are the unit vectors along the corresponding coordinates. For the configurations in formula (45), the cylindrical components of the magnetization do not depend on the angle ϕ. For such configurations, rotation along the z axis and a simultaneous rotation of the vector $\mathbf{M}$ leaves the configuration invariant. This is an example of an *equivariant* configuration. For simplicity, we will sometimes also call this configuration *axially-symmetric*.

We proceed to write the solution of the Poisson equation solution for the configuration (45). For this purpose, the radial distance needs to be written in terms of the cylindrical coordinates,

$$r = \sqrt{x^2 + y^2 + z^2} \Rightarrow r = \sqrt{\rho^2 \cos^2\phi + \rho^2 \sin^2\phi + z^2} \Rightarrow r = \sqrt{\rho^2 + z^2}.$$

Eq. (40) reduces to

$$\psi = -\int_V \frac{\nabla \cdot \mathbf{M}(\mathbf{r}')}{|\mathbf{r} - \mathbf{r}'|} dV' \Rightarrow \psi = -\int_V \frac{\nabla \cdot \mathbf{M}(\mathbf{r}')}{\sqrt{(\mathbf{r} - \mathbf{r}')^2}} dV' \Rightarrow \psi = -\int_V \frac{\nabla \cdot \mathbf{M}(\mathbf{r}')}{\sqrt{\mathbf{r}^2 + \mathbf{r}'^2 - 2\mathbf{r}\cdot\mathbf{r}'}} dV'$$

$$\Rightarrow \psi = -\int_V \frac{\nabla \cdot \mathbf{M}(\rho', z')}{[\rho^2 + z^2 + \rho'^2 + z'^2 - 2(\rho^2 + z^2)(\rho'^2 + z'^2)]^{1/2}} \rho' d\rho' dz' d\phi'$$

$$\Rightarrow \psi = -\int_V \frac{\nabla \cdot \mathbf{M}(\rho', z')}{\left[\rho^2 + z^2 + \rho'^2 + z'^2 - 2(\rho \cdot \rho' + \cancelto{0}{\mathbf{z}\cdot\boldsymbol{\rho}'} + \cancelto{0}{\mathbf{z}'\cdot\boldsymbol{\rho}} + \mathbf{z}\cdot\mathbf{z}')\right]^{1/2}} \rho' d\rho' dz' d\phi'$$

$$\Rightarrow \psi = -\int_V \frac{\nabla \cdot \mathbf{M}(\rho', z')}{[\rho^2 + z^2 + \rho'^2 + z'^2 - 2\rho\rho'\cos\phi' - 2zz']^{1/2}} \rho' d\rho' dz' d\phi'.$$

Finally, the following is obtained

$$\psi(\rho, z) = -\iint \nabla \cdot \mathbf{M}(\rho', z') \rho' d\rho' dz' \int \frac{d\phi'}{[\rho^2 + \rho'^2 - 2\rho\rho'\cos\phi' + (z - z')^2]^{1/2}} \tag{46}$$

where the integration extends over the space where $\mathbf{M} \neq 0$. This is the formula used in the simpler case of (44).

4.2.1 The case of zero azimuthal component

Let us assume a magnetization configuration of the form

$$\mathbf{M}(\rho, z) = M_\rho(\rho, z)\hat{\mathbf{e}}_\rho + M_z(\rho, z)\hat{\mathbf{e}}_z \tag{47}$$

that is axially symmetric and has no component in the azimuthal direction. Consider the form

$$\mathbf{M}(\rho, z) = \frac{1}{\rho} e^{\frac{-a}{\rho}} \hat{\mathbf{e}}_\rho + k\,\hat{\mathbf{e}}_z \tag{48}$$

with $a > 0$, indicating a scale at which the the magnetization goes to zero for the radial part. This magnetization is getting larger in the polar radial coordinate until it drops rapidly after a threshold. Then, only the z- part of the magnetization remains and it resembles the the configuration in Chapter (4.1). Maybe, a similar magnetization appears near and inside a copper wire.

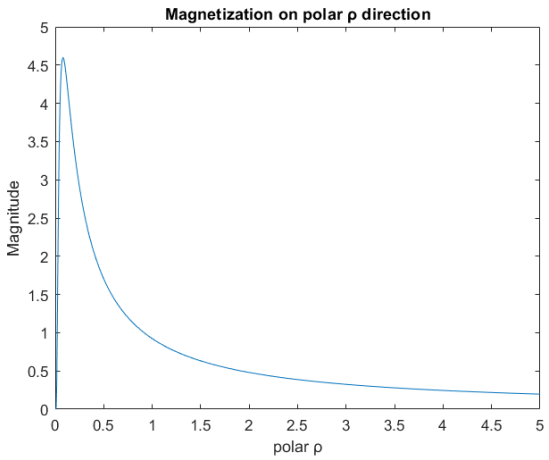

Figure 14: Magnetization magnitude on the polar coordinate shown to peak and then drop rapidly for $a = 0.1$. This relation is chosen to model the fast drop of the magnitude inside the cylindrical source.

The Poisson equation can be derived

$$\Delta\psi = \nabla \cdot \mathbf{M} \Rightarrow \Delta\psi = \frac{a\mathrm{e}^{\frac{-a}{\rho}}}{\rho^3}\,. \tag{49}$$

For the source, it's assumed that $k = 1$ and the same z-axis orientation as in Chapter (4.1). For this model, the radial part of the magnetization will decrease fast enough for it to be small but not zero at the boundary. As such, depending on $a = 10$, the radius $R = 0.1$ will be chosen appropriately.
The volume part of solution is

$$\psi_{vol} = -a \iint \frac{\mathrm{e}^{\frac{-a}{\rho'}}}{\rho'^2}\, d\rho' dz' \int \frac{d\phi'}{(\rho^2 + \rho'^2 - 2\rho\rho'\cos\phi' + (z - z')^2)^{1/2}}. \tag{50}$$

From the surface integral there are three parts

$$\psi_{surf}(\rho, z) = \oint_S \frac{\mathbf{M}(\mathbf{r}') \cdot \mathbf{dS}'}{|\mathbf{r} - \mathbf{r}'|}$$

$$\Rightarrow \psi(\rho, z)_{surf} = \oint_{top\,cap} \frac{\mathbf{M}(\mathbf{r}') \cdot \mathbf{dS}'}{|\mathbf{r} - \mathbf{r}'|} + \oint_{lower\,cap} \frac{\mathbf{M}(\mathbf{r}') \cdot \mathbf{dS}'}{|\mathbf{r} - \mathbf{r}'|} + \oint_{cylinder} \frac{\mathbf{M}(\mathbf{r}') \cdot \mathbf{dS}'}{|\mathbf{r} - \mathbf{r}'|}$$

$$\begin{aligned}
\psi_{bottom} &= -\int_0^R \int_0^{2\pi} \frac{k\rho'\, d\rho' d\phi'}{(\rho^2+\rho'^2-2\rho\rho'\cos\phi'+(z-z_a)^2)^{1/2}} \\
\psi_{top} &= \int_0^R \int_0^{2\pi} \frac{k\rho'\, d\rho' d\phi'}{(\rho^2+\rho'^2-2\rho\rho'\cos\phi'+(z-z_b)^2)^{1/2}} \\
\psi_{cylinder} &= \int_0^{2\pi} \int_{z_a}^{z_b} \frac{e^{\frac{-a}{R}}\, dz' d\phi'}{(\rho^2+R^2-2R\rho\cos\phi'+(z-z')^2)^{1/2}}.
\end{aligned} \tag{51}$$

All three integrals need to be approximated at the boundary nodes with MC. Using a mesh of 534 boundary nodes, 4764 in total, the field can be calculated. This time, the field is

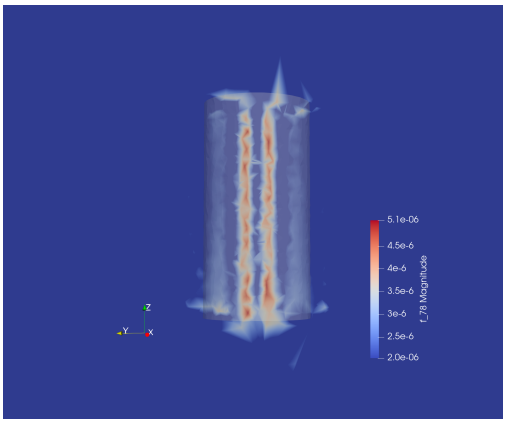

(a) Magnitude of field on z-y pane

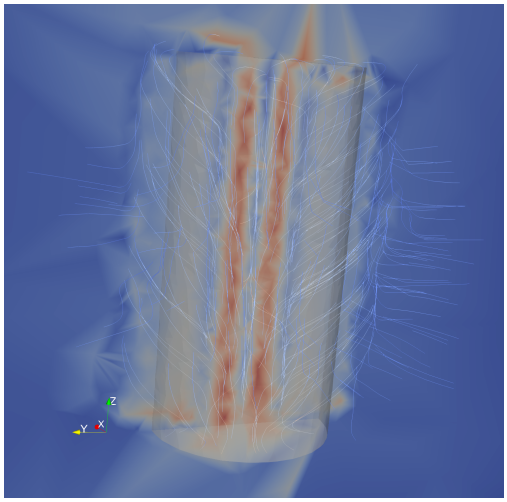

(b) Field lines visualized in 3D space of Magnetic field

Figure 15: Values of the B magnetic field generated by the case of zero azimuthal component of magnitude shown in Fig.(14) for the polar coordinate; and a homogeneous one for the z coordinate. The values are derived through a Poisson BVP. It was approximated in a mesh of 4764 nodes, 534 of which were on the boundary of the domain. The approximations of the boundary values were made with 150 MC iterations.

measured inside the source, too. Therefore, Fig.(15) is the B-field. The values from FEM represent the H-field. That is then used to get B through Eq.(5). The axial symmetry is present as expected. The field far away from the source should resembles that of Chapter (4.1), if the radial part goes down fast enough. The numbers are chosen so there is some radial part remaining at the surface of the source. Thus, inside of it, the field lines behave as in Fig.(15b).

4.3 Toroidal Source

Another bundle of problems, that have their own strong symmetry, similar to the cylinder, is that of the torus source.

The parametric equations for the torus, with the origin as its center, are , Ref.[27]:

$$\begin{aligned} x &= (R + r_0 \cos v) \cos u \\ y &= (R + r_0 \cos v) \sin u \\ z &= r_0 \sin v. \end{aligned} \tag{52}$$

With $u, v \in (0, 2\pi)$, R the radius from the center of the hole to the center of the torus and r_0 the radius of the tube. The way u and v are defined will indicate the orientation of the torus. If they are the spherical θ, ϕ coordinates, the axis of revolution is the z-axis. The surface element and the volume element will also be needed for the transformation of the integrals. From calculus,

$$d\mathbf{A} = r_0(R + r_0 \cos v)\big(\cos u \cos v, \sin u \cos v, \sin v\big) du dv \tag{53}$$

and

$$dV = r(R + r \cos v)\, dr dv du. \tag{54}$$

4.3.1 Azimuthal term without azimuthal variation

Choosing the magnetization

$$\mathbf{M} = f(\rho, z)\hat{\mathbf{e}}_\phi. \tag{55}$$

the Poisson equation is derived

$$\Delta\psi = \nabla \cdot \mathbf{M} \Rightarrow \Delta\psi = 0. \tag{56}$$

The solution of the Poisson equation is

$$\psi = \oint_S \frac{\mathbf{M}(\mathbf{r}') \cdot \mathbf{dS}'}{(|\mathbf{r} - \mathbf{r}'|} = 0 \tag{57}$$

since the normal vector of the toroidal surface is always vertical to a magnetization that has only an azimuthal term. So the magnetic field is zero everywhere.

4.3.2 Only radial term

Torus shaped magnets are sometimes used in construction and ring-like magnets are also occasionally used in medicine.

Provided this magnetization:

$$\mathbf{M} = \hat{\mathbf{e}}_\rho. \tag{58}$$

The Poisson equation is derived

$$\Delta\psi = \nabla \cdot \mathbf{M} \Rightarrow \Delta\psi = \frac{1}{\rho}. \tag{59}$$

Using Eq.(54) and Eq.(53) the solution of the Poisson problem is

$$\psi_{vol} = -\int_V \frac{\nabla \cdot \mathbf{M}(\mathbf{r}')}{|\mathbf{r} - \mathbf{r}'|} dV' \Rightarrow$$

$$\psi_{vol}(x, y, z) = -\int_0^{2\pi}\int_0^{2\pi}\int_0^{r_0} \frac{r' dr' dv du}{\sqrt{[x - \cos u(R + r' \cos v)]^2 + [y - \sin u(R + r' \cos v)]^2 + [z - r' \sin v]^2}} \tag{60}$$

and

$$\psi_{surf} = \oint_S \frac{\mathbf{M}(\mathbf{r}') \cdot dS'}{|\mathbf{r} - \mathbf{r}'|} \Rightarrow$$

$$\psi_{surf}(x.y,z) = \int_0^{2\pi}\int_0^{2\pi} \frac{r_0(R + r_0\cos v)\big(\cos u, \sin u, 0\big) \bullet \big(\cos u\cos v, \sin u\cos v, \sin v\big)}{|\mathbf{r} - \mathbf{r}'|} dvdu \Rightarrow$$

$$\psi_{surf}(x,y,z) = \int_0^{2\pi}\int_0^{2\pi} \frac{r_0\cos v(R + r_0\cos v)}{\sqrt{[x - \cos u(R + r_0\cos v)]^2 + [y - \sin u(R + r_0\cos v)]^2 + [z - r_0\sin v]^2}} dvdu. \quad (61)$$

The mesh used has a torus shaped hole where the source would be, 7860 nodes with 693 on the boundary.

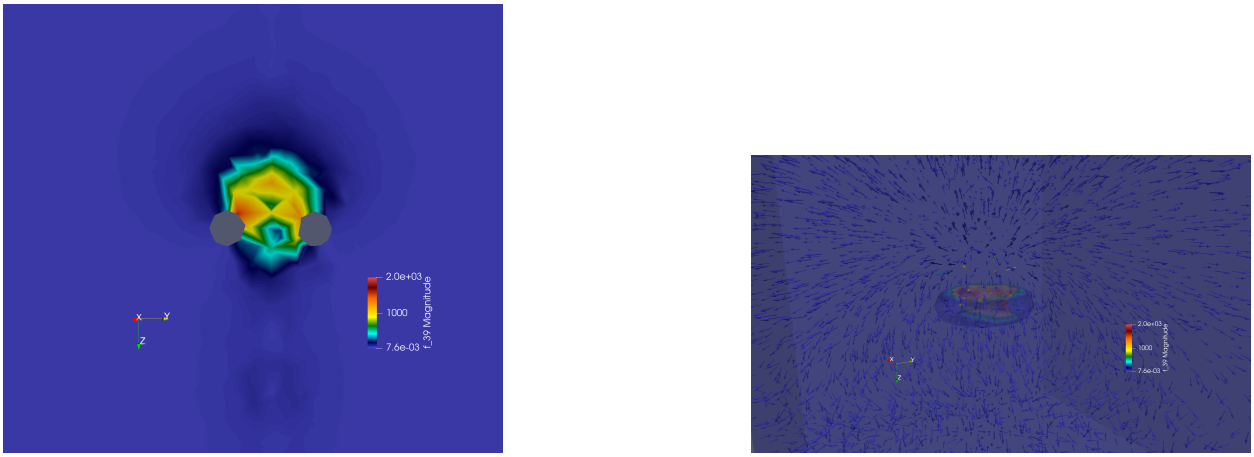

(a) Magnitude on y-z plane

(b) Field lines visualized in 3D space

Figure 16: Values of the H magnetic field generated by toroidal source of $R = 0.5, r = 0.2$ centered at (0,0,0) and oriented on z-axis. The field is created by the magnetization described in Eq.(55). The values are derived through a Poisson BVP. It was approximated in a mesh of 7860 nodes, 693 of which were on the boundary of the domain. The approximations of the boundary values were made with 200 MC iterations.

This is once again the H-field generated. The solution bears the axial symmetry and generates relatively high magnitudes close to the source. The field lines far away from the source behave like a dipole, Yet, coming closer, there appears to be a preference for one side of the z-axis. This might need more investigation as it maybe is a numerical error.

4.4 Localised axially symmetric "Cloud" configuration

To end this Chapter, a configuration for a more generalised case of source is devised. Knowing the magnetization and assuming a "cloud of sources" in a radius of r_0, the problem inside and outside this source can be defined.

A more general axially symmetric magnetization is chosen.

$$\mathbf{M}(\rho, z) = M_\phi(\rho, z)\hat{\mathbf{e}}_\phi + M_z(\rho, z)\hat{\mathbf{e}}_z$$

with

$$\lim_{(\rho,z)\to\infty} \mathbf{M}(\rho, z) = 0$$

and with $|\mathbf{M}| = 1$ for $\{\rho, z\} = \{0, 0\}$.
An example of such a function is

$$\mathbf{M}(\rho, z) = \frac{\sqrt{2}}{2}\ e^{-\frac{1}{a(\rho^2+z^2)}}\hat{\mathbf{e}}_\phi + \frac{\sqrt{2}}{2}\ e^{-\frac{1}{a(\rho^2+z^2)}}\hat{\mathbf{e}}_z \tag{62}$$

with $a \geq 1$, a factor that defines how fast the magnetization drops going away from the origin . An appropriate a is chosen, so $\mathbf{M}$ drops fast enough for us to assume that the surface integral is zero. This choice changes according to how big is the source cloud.

The Poisson equation is

$$\Delta\psi = \nabla \cdot \mathbf{M} \Rightarrow \Delta\psi = \frac{-\sqrt{2}z}{a(\rho^2+z^2)^2}\ e^{-\frac{1}{a(\rho^2+z^2)}}. \tag{63}$$

The solution of the Poisson equation is

$$\psi_{vol} = -\int_V \frac{\nabla \cdot \mathbf{M}(\mathbf{r}')}{|\mathbf{r}-\mathbf{r}'|}dV' \Rightarrow \psi_{vol} = -\iiint \frac{\frac{-\sqrt{2}z}{ar^4}\ e^{-\frac{1}{ar^2}}}{|\mathbf{r}-\mathbf{r}'|}dV' \Rightarrow$$

$$\psi_{vol}(x, y, z) = \sqrt{2}\int_0^{\pi}\int_0^{2\pi}\int_0^{r_0} \frac{e^{\frac{1}{-ar'^2}}\sin(\phi')\cos(\phi')}{ar'\,|\mathbf{r}-\mathbf{r}'|}dr'd\theta'd\phi' \tag{64}$$

and

$$\psi_{surf}(x, y, z) = 0 \tag{65}$$

given that the magnetization is assumed to be zero on the boundary of the cloud.

The mesh used has 5996 nodes with 1052 on the boundary. Once again, since we model

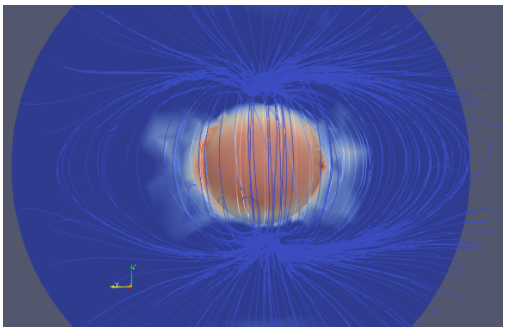

(a) Field lines visualized in 3D space

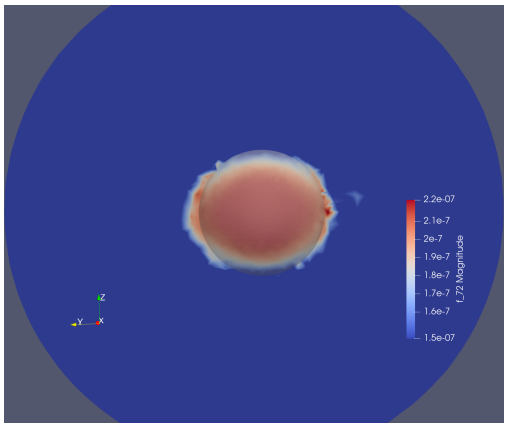

(b) Magnitude on z-y plane

Figure 17: Values of the B magnetic field generated by axially symmetric "Cloud" of radius $r_0 = 0.5$ centered at (0,0,0). The field is created by the magnetization described in Eq.(62) of scale value $a = 10$. The values are derived through a Poisson BVP. It was approximated in a mesh of 5996 nodes, 1052 of which were on the boundary of the domain. The approximations of the boundary values were made with 100 MC iterations.

values inside the source, we'll transform the solution to represent the B-field. Looking at Fig.(17), the results are invariant to rotations around z-axis and have a slight preference on the polar radial direction. Consider that the assumption is that the surface integral does not contribute. If we were to enforce a homogeneous value on the surface of the 'cloud', the field lines of the equations in Chapter (2) would appear.

5 Hopfions

Definition 5.1 (The Hopf index)**.** Suppose two points a and b in a two dimensional sphere S^2. For a suitably smooth map $f : S^3 \to S^2$, $f^{-1}(a)$ and $f^{-1}(b)$ will be a set of closed curves in S^3. We define the Hopf index as the number of intersections between $f^{-1}(a)$ and the closed, connected and oriented surface $\Sigma \in S^3$ with boundary $f^{-1}(b)$. Just for this text, we'll call such intersections, *Hopfian*. Furthermore, the index is independent of the choice of Σ, a or b. And it remains the same, even for continual deformations of the map f, Ref.[5]. Thus, the Hopf index divides maps $S^3 \to S^2$ into classes that are disjointed since the maps of different Hopf indices cannot be deformed into each other.

The index appears to be a defining invariant for the type of problems that are described in Definition (5.1). It characterizes the homotopy of the continuous mapping from the unit ball to the unit sphere. In addition, this number is a unique characteristic of the topology. Which means that different configurations, of the same index, can be transformed into each other by a continuous deformation.

For a unit vector $\mathbf{n}(\mathbf{r}) = \mathbf{n}(x, y, z)$ with $\mathbf{n}^2 = 1$ and an existing limit at infinity, the Hopf index is defined from the formula

$$H = -\frac{1}{(8\pi)^2} \int \mathbf{F} \cdot \mathbf{A} d\mathbf{r}. \tag{66}$$

The above are defined as

$$\begin{aligned} F_i =& \epsilon_{ijk} \mathbf{n} \cdot (\nabla_j \mathbf{n} \times \nabla_k \mathbf{n}) \\ \mathbf{F} =& \nabla \times \mathbf{A}. \end{aligned} \tag{67}$$

where the Levi-Civita symbol is used and a summation over the indices is depicted. However, a more geometric approach will be adopted for finding the Hopf index below.

5.1 Hopf index unity

The author in Ref. [4] uses the following family of magnetizations for the purpose of investigating the existence of axially symmetric 3D solitons in ferromagnetic matter. A stereographic projection can correlate all points of a plane, including infinity, to a sphere. Similarly, there is a correlation between all points of the real space to a ball. Thus,

$$\Omega = \frac{(M_1 + iM_2)}{1 + M_3} = \frac{2\alpha\rho e^{i\phi}}{2\alpha z + i(\rho^2 + z^2 - \alpha^2)} \tag{68}$$

where (ρ, ϕ, z) are the usual cylindrical coordinates and α an arbitrary scale parameter. In Ref.[4], this magnetization is specifically wanted to have Hopf index equal to unity. Inverting

the above relation and using $\alpha = 1$ to find

$$M_1 = \frac{\Omega + \overline{\Omega}}{1 + \Omega\overline{\Omega}}, \quad M_2 = \frac{1}{i}\frac{\Omega - \overline{\Omega}}{1 + \Omega\overline{\Omega}}, \quad M_3 = \frac{1 - \Omega\overline{\Omega}}{1 + \Omega\overline{\Omega}} \tag{69}$$

and

$$\bullet 1 + \Omega\overline{\Omega} = 1 + \frac{2\rho e^{i\phi}}{2z + i(\rho^2 + z^2 - 1)}\frac{2\rho e^{-i\phi}}{2z - i(\rho^2 + z^2 - 1)} = 1 + \frac{4\rho^2}{4z^2 + (\rho^2 + z^2 - 1)^2}$$

$$\bullet \Omega + \overline{\Omega} = \frac{2\rho e^{i\phi}}{2z + i(\rho^2 + z^2 - 1)} + \frac{2\rho e^{-i\phi}}{2z - i(\rho^2 + z^2 - 1)} = \frac{4z\rho[e^{i\phi} + e^{-i\phi}] + i2\rho(\rho^2 + z^2 - 1)[-(e^{i\phi} - e^{-i\phi})]}{4z^2 + (\rho^2 + z^2 - 1)^2}.$$

Substituting in (69),

$$M_1 = 4\rho\frac{2z\cos(\phi) + (\rho^2 + z^2 - 1)\sin(\phi)}{4z^2 + 4\rho^2 + (\rho^2 + z^2 - 1)^2} \Rightarrow$$

$$M_1 = 4\rho\frac{2z\cos(\phi) + (\rho^2 + z^2 - 1)\sin(\phi)}{(\rho^2 + z^2 + 1)^2}.$$

Similarly,

$$M_2 = 4\rho\frac{2z\sin(\phi) - (\rho^2 + z^2 - 1)\cos(\phi)}{(\rho^2 + z^2 + 1)^2}$$

and

$$M_3 = \frac{4z^2 + (\rho^2 + z^2 - 1)^2 - 4\rho^2}{4z^2 + (\rho^2 + z^2 - 1)^2 + 4\rho^2}.$$

Finally,

$$\begin{aligned} M_1 &= 4\rho\frac{2z\cos(\phi) + (\rho^2 + z^2 - 1)\sin(\phi)}{(\rho^2 + z^2 + 1)^2} \\ M_2 &= 4\rho\frac{2z\sin(\phi) - (\rho^2 + z^2 - 1)\cos(\phi)}{(\rho^2 + z^2 + 1)^2} \\ M_3 &= 1 - \frac{8\rho^2}{(\rho^2 + z^2 + 1)^2}. \end{aligned} \tag{70}$$

To easily find the index, using to the Definition 5.1, we suggest some appropriate a and b or $\mathbf{M_a}$ and $\mathbf{M_b}$. Considering the index remains the same for the same map and its continuous deformations, only one pair of a and b is needed. Substituting the below values on Eq.(70) we get

$$\begin{aligned} \rho = 0 &\Rightarrow \mathbf{M}_a = (0, 0, 1) \\ \rho = 1, z = 0 &\Rightarrow \mathbf{M}_b = (0, 0, -1). \end{aligned} \tag{71}$$

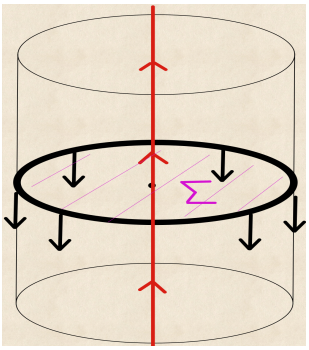

Figure 18: With $\mathbf{M_a^{-1}}$(red) and $\mathbf{M_b^{-1}}$(black) we represent the closed vortex lines that have constant magnetization $\mathbf{M_a}$ and $\mathbf{M_b}$, respectively. Σ indicates the surface of boundary $\mathbf{M_b^{-1}}$, similarly to the Definiton 5.1. Seemingly, $\mathbf{M_a^{-1}}$ intersects only once with Σ, demonstrating that the Hopf index is unity.

Figure (18) implies that there is only one intersection between the plane Σ and this z-axis line. Using the approach of the stereographic projection, $\mathbf{M_a^{-1}}$ can be thought of as a closed line by identifying all points at infinity where the magnetization also approaches the state $\mathbf{M_a}$.

A more detailed understanding is obtained by recalling that the complex variable Ω is chosen to remain constant along each vortex line. So,

$$\Omega = Ce^{i\phi_0} \tag{72}$$

for $0 \leq \phi_0 \leq 2\pi$, and like above

$$\begin{aligned}
&\Rightarrow \frac{2\alpha\rho e^{i\phi}}{2\alpha z + i(\rho^2 + z^2 - \alpha^2)} = Ce^{i\phi_0} \\
&\Rightarrow 2\alpha\rho e^{i(\phi-\phi_0)} = C[2\alpha z + i(\rho^2 + z^2 - \alpha^2)] \\
&\Rightarrow e^{i(\phi-\phi_0)} = C[\frac{z}{\rho} + i\frac{\rho^2 + z^2 - \alpha^2}{2\alpha\rho}.]
\end{aligned}$$

From the imaginary part

$$\sin(\phi - \phi_0) = C\frac{\rho^2 + z^2 - \alpha^2}{2\alpha\rho} \tag{73}$$

and from the real part

$$\cos(\phi - \phi_0) = C\frac{z}{\rho}. \tag{74}$$

Combining them,

$$\Rightarrow \tan(\phi - \phi_0) = \frac{\rho^2 + z^2 - \alpha^2}{2\alpha z}. \tag{75}$$

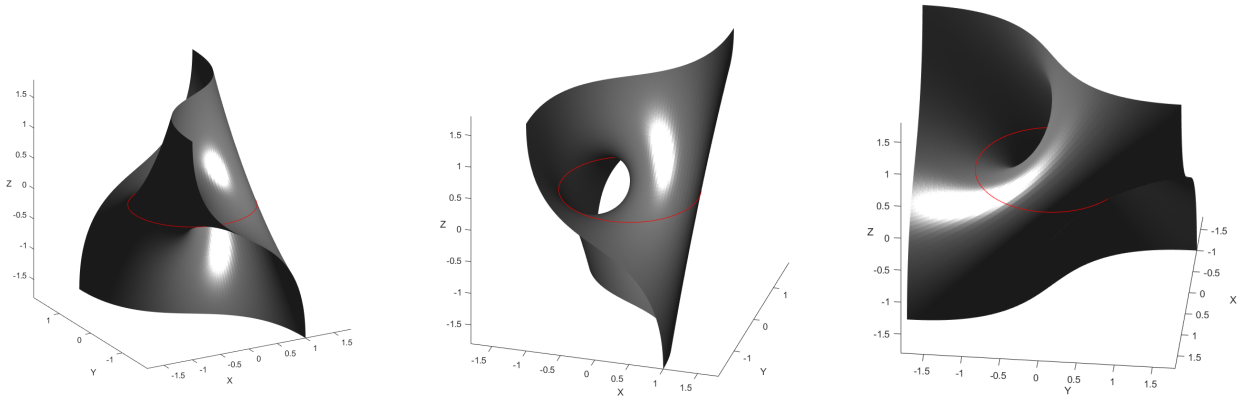

Figure 19: Eq.(75) for $\{a = 1,\ \phi_0 = 0\}$ (grey) shown from 3 angles. Above, $\mathbf{M_b^{-1}}$(red) is demonstrated to be part of the equation. And it is, indeed, for every ϕ_0. For a different value of a, both the surface and the curve scale with it. But, they always have the same geometric relation.

Choosing the constant $C^2 = \frac{a^2}{c^2-a^2}$, for $c \geq a$

$$\sin^2(\phi-\phi_0)+\cos^2(\phi-\phi_0)=1 \Rightarrow C^2[\frac{(\rho^2+z^2-\alpha^2)^2}{4a^2\rho^2}+\frac{z^2}{\rho^2}]=1$$
$$\Rightarrow z^2+\frac{(\rho^2+z^2-\alpha^2)^2}{4a^2}=\frac{\rho^2}{C^2}$$
$$4z^2+a^2-2\rho^2-2z^2+\frac{\rho^4+z^4+2\rho^2z^2}{a^2}=\frac{4\rho^2}{C^2}\Rightarrow$$
$$\Rightarrow a^2-2\rho^2+2z^2+\frac{\rho^4+z^4+2\rho^2z^2}{a^2}=\frac{4\rho^2(c^2-a^2)}{a^2}$$
$$\Rightarrow z^4+\rho^4+a^4+2a^2\rho^2+2a^2\rho^2+2a^2z^2=4\rho^2c^2$$
$$\Rightarrow (\rho^2+z^2+a^2)^2=(2\rho c)^2$$

and given that ρ and c are always non-negative

$$\rho^2+z^2+a^2=2\rho c \Rightarrow \rho^2-2\rho c+c^2+z^2=c^2-a^2$$
$$\Rightarrow (\rho-c)^2+z^2=c^2-a^2. \tag{76}$$

Equations (75) and (76) are true for fixed $c \geq a$, as the radius goes from the center of the hole to the center of the torus tube and $0 \leq \phi_0 \leq 2\pi$. The intersections of the 2 surfaces describe the vortex lines of the magnetization.

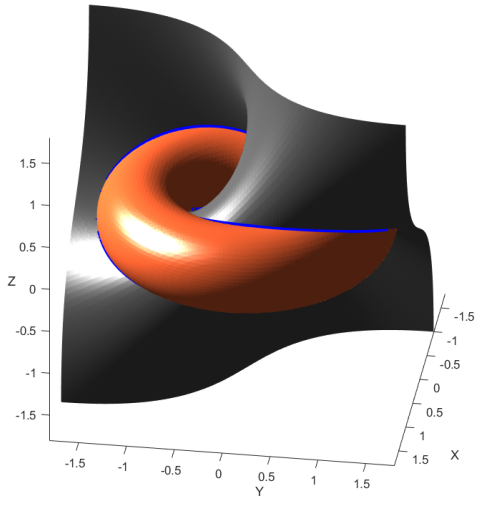

(a) Eq.(75) with $\{a = 1, \phi_0 = 0\}$(grey) and Eq.(76) with $c = 1$(orange)

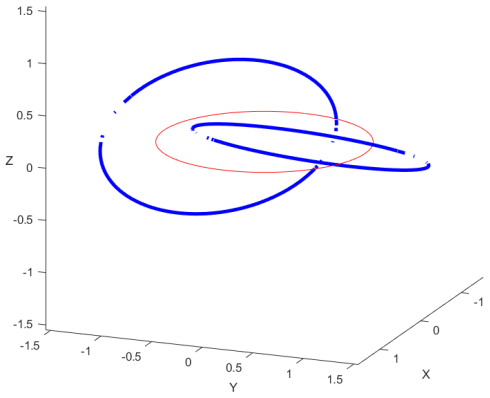

(b) Intersections of Eq.(75) and Eq.(76)(blue) and $\mathbf{M_b^{-1}}$(red)

Figure 20: Eq.(75) and Eq.(76) with their common points' curves. These curves indicate the vortex of the magnetization. Also, those curves have only one of those Hopfian intersections that are described in Definition(5.1). This, further demonstrates that the magnetization has Hopf index equal to 1.

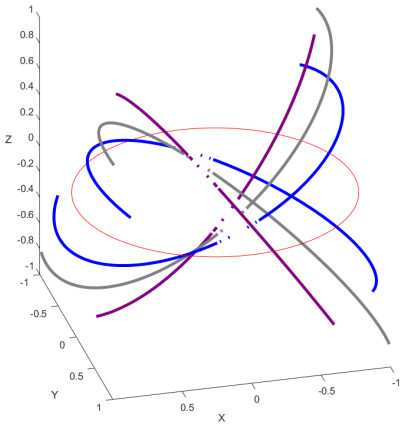

Figure 21: Common points of Eq.(75) and Eq.(76) for some different c-values and $\mathbf{M_b^{-1}}$(red) showing their Hopfian intersection is unity for any couple of curves chosen.

As shown above, for any fixed c, the vortex lines are confined on the surface of the torus. Which they cover completely, as the constant ϕ_0 of Eq.(75) varies through its interval. Also, the common points of Eq.(75) and Eq.(76) give a pair of curves. And even those two curves have only one Hopfian intersection with each other. Essentially, all the vortex lines are closed. And the number of Hopfian intersections of any couple of them is equal to unity. That holds for any c or ϕ_0. Additionally, the smaller the difference $c^2 - a^2$ becomes, the closer the 2 curves move. In the limit that the mentioned difference becomes zero, the equations collapse and the points merge to become $\mathbf{M_b^{-1}}$.

5.2 Holf index zero

We modify the stereographic variable to not depend on the azimuthial angle term. We hypothesise, that a configuration of Hopf index of zero emerges. Which implies that there are no Hopfian intersections between any closed curves of the vortex, as presented in Definition 5.1.

$$\Omega = \frac{(M_1 + iM_2)}{1 + M_3} = \frac{2\alpha\rho}{2\alpha z + i(\rho^2 + z^2 - \alpha^2)}. \tag{77}$$

The magnetization is

$$\begin{aligned} M_1 &= \frac{8a^2\rho z}{(\rho^2 + z^2 + a^2)^2} \\ M_2 &= -\frac{4\rho a(\rho^2 + z^2 - a^2)}{(\rho^2 + z^2 + a^2)^2} \\ M_3 &= 1 - \frac{8a^2\rho^2}{(\rho^2 + z^2 + a^2)^2} \end{aligned} \tag{78}$$

and as above the Eqs.(75), (76) of this configuration, respectively, are

$$\begin{aligned} &\tan(\phi_0) = \frac{\rho^2 + z^2 - \alpha^2}{2\alpha z} \Rightarrow \\ &(\rho - c)^2 + z^2 = c^2 - a^2 \end{aligned}$$

$$\begin{aligned} &\rho^2 + (z - \tan(\phi_0))^2 = a^2(1 - \tan^2(\phi_0)) \\ &(\rho - c)^2 + z^2 = c^2 - a^2. \end{aligned} \tag{79}$$

For fixed c, a, ϕ_0 they correspond to sphere and a torus as shown in Fig.(22a).

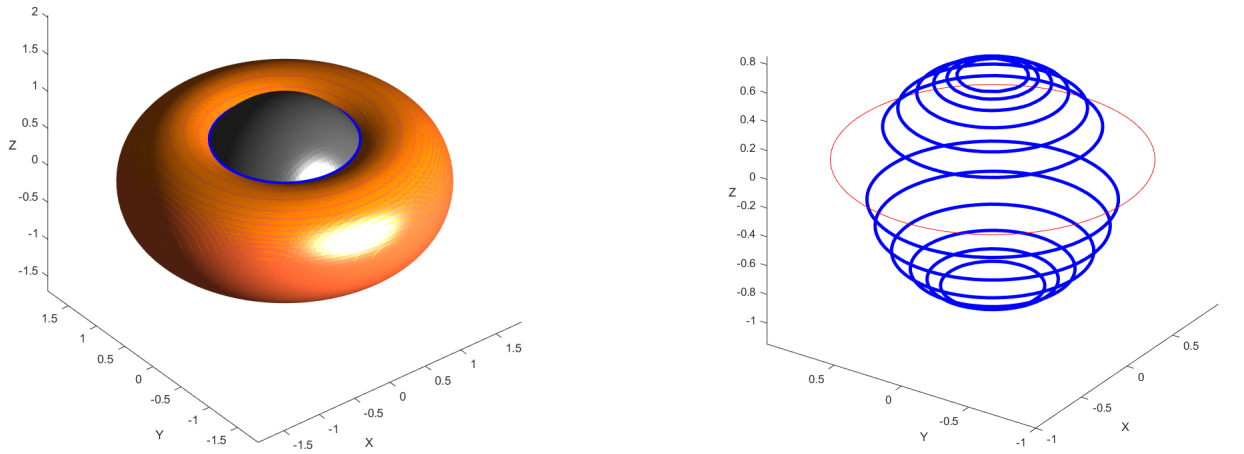

(a) Eq.(79) for $\{a = 1, c = 1.2, \phi_0 = 0\}$(orange & grey) and their intersections(blue)

(b) Intersections of Eq.(79) for several different c values (blue) and $\mathbf{M_b^{-1}}$(red)

Figure 22: Surfaces of Equations (79) and their common points' curves. Also, those lines have zero Hopfian intersections with each other. This demonstrates that the magnetization has Hopf index equal to 0.

From Fig.(22), we deduce that there are no Hopfian intersections between the common points of those surfaces. They appear to be concentric circles. And that remains true for all choices of ϕ_0 and c as none of those couples generate the same curve, as described on Eq.(79).

6 Suggestions

We'd like to close with some suggestions that would greatly change the traction of the above methods. We estimate that a dramatic difference will be observed, if we were to carefully choose the FE method. Lagrange's elements method is useful but one of the simpler FEM. It would be interesting to see what are the benefits of other methods like Hermitian elements, Quadrature, Crouzeix-Raviart, to name a few. Also, maybe the convergence could vary for a range of problems. Recall that this is an effortless change with FEniCS, for anyone to follow up.

Another improvement, that could be applied, is a more efficient MC integration method namely some importance sampling as presented in Ref.[15]. Faster and more accurate convergence supplies additional hardware space to employ on more nodes; and more faithful boundary conditions to follow from.

Furthermore, this thesis' approach of error measurement, although mostly reliable, is simplistic. Firstly, There was not a division nor an analysis between discretization and numerical errors. The first arise from the creation of the mesh and the other from the solution of the FE system equations. This could be truly informative for where to focus the work for better simulations. Moreover, the density of the grid chosen for each simulation is essentially empirical. We choose a dense grid near the area close to the source gradually changing it to a less so, away from the source. The exact grid numbers used for each simulation are a choice of multiple iterations trying to minimize the error, although no rigorous optimization method was used.

Additionally, the magnetic configurations were specifically chosen so the equations could be analytically simplified. While indicated, there's no assurance that the methods will converge as fast in an extremely non symmetric problem. To conclude, the focus of this thesis was to study many different mathematical configurations. The tools described herein can be developed to address more experimental paradigms. Those coveted boundary values can be procured experimentally or be interpolated by data. In the case of unknown magnetization but known boundary values a solution can be approximated for specific cases and domains.

7 References

[1] Jackson, John David (1999). *Classical electrodynamics (3rd ed.)*. New York: Wiley.

[2] Griffiths, David J. (1998). *Introduction to Electrodynamics (3rd ed.)*. Prentice Hall.

[3] Browne, Michael (2008). *Physics for Engineering and Science (2nd ed.)*. McGraw-Hill/Schaum.

[4] Greg Baker, Saleh Tanveer (auth.), Russel E. Caflisch, George C. Papanicolaou (eds.) - *Singularities in Fluids, Plasmas and Optics*, Chapter: Dynamics of Magnetic Vortex rings (1993, Springer Netherlands),[NATO ASI Series 404]

[5] Nicole D.A., *Solitons with non-vanishing Hopf index*, University of Southampton, 1978

[6] Dzyloshinskii I.E., Ivanov B.A., *Localized topological solitons in a ferromagnet*, USSR & UkrSSR Academy of Science, 1979

[7] Evans, L. C. (1998). *Partial Differential Equations*. Providence: American Mathematical Society.

[8] Kira Seleznyova, Mark Strugatsky, Janis Kliava. *Modelling the magnetic dipole*. European Journal of Physics, European Physical Society, 2016, 37 (2), pp.025203 (1-14). ¡10.1088/0143- 0807/37/2/025203

[9] Charalambopoulos A., *Laplace equation in the exterior of a convex polygon*, University of Ioannina,

[10] H. Brezis. *Functional Analysis, Sobolev Spaces and Partial Differential Equations*. Springer. 2010.

[11] Green, George. *An Essay on the Application of Mathematical Analysis to the Theories of Electricity and Magnetism*, Nottingham, 1828.

[12] Q. Han, F. Lin. *Elliptic Partial Differential Equations*. AMS. 1997.

[13] L. Beirao da Veiga, F. Dassi, A. Russo, *A C^1 Virtual Element Method on polyhedral meshes*, University of Milano - Bicocca, 2019

[14] Gatica, Gabriel. (2018). *A note on stable Helmholtz decompositions in 3D*. Applicable Analysis. 99. 1-12.

[15] Ping Wang, *Modified Monte Carlo method for triple integral*, Qingdao University, International Conference of Information Technology, 2011

[16] R . Courant, *Variational methods for the solution of problems of equilibrium and vibrations*, 1943

[17] Jacob Fish and Ted Belytschko, *A First Course in Finite Elements by Jacob Fish and Ted Belytschko*, Wiley, 2007

[18] K . Schellbach, *Probleme der Variationsrechnung*(translated), 1851, Berlin

[19] Y. F. Gui and W. B. Dou, *A rigorous and completed statement on Helmhotz theorem*, Southeast University, 2007

[20] Yuanyuan Liana, Kai Zhanga, Dongsheng Lib, Guanghao Hong, *Boundary Hölder Regularity for Elliptic Equations*, Northwestern Polytechnical University, Xi'an, Shaanxi, 2020

[21] Barkanov E, *Introduction to the Finite Elements* Riga University, 2001

[22] HP Meyers (1997). *Introductory solid state physics (2 ed.)*. CRC Press.

[23] Komineas, S., Charmandaris, E., 2016. *Mathematical Modeling*. [ebook] Athens:Hellenic Academic Libraries

[24] O.C. Zienkiewicz, R.L. Taylor and J.Z. Zhu, *The Finite Element Method: Its Basis and Fundamentals*, McGraw-Hill, 1967

[25] Em A., Guermond J.L., *Theory and Practice of Finite Elements*, Applied Mathematical Sciences, Volume 159, 2004

[26] Nick T. Thomopoulos, *Essentials of Monte Carlo Simulation: Statistical Methods for Building Simulation Models*, Springer,ed,2013

[27] Harris, J. W. and Stocker, H. "Torus." §4.10.5 in *Handbook of Mathematics and Computational Science*. New York: Springer-Verlag, p. 113, 1998.

[28] Schopf M., *Error analysis of the Galerkin FEM in L2-based norms for problems with layers*. PhD Dissertation, University of Dresden, 2014

[29] *Ferromagnetism*, Feynman Lectures in Physics Ch 36

[30] *The magnetism of matter*, Feynman Lectures in Physics Ch 34

[31] Gonano, Carlo and Zich, Riccardo and Mussetta, Marco *Definition for Polarization P and Magnetization M Fully Consistent with Maxwell's Equations*, Progress In Electromagnetics Research B, volume 64, 2015

[32] *Law of large numbers*, Encyclopedia of Mathematics, EMS Press, 2001

[33] C. Geuzaine and J.-F. Remacle. *Gmsh: a three-dimensional finite element mesh generator with built-in pre- and post-processing facilities*. International Journal for Numerical Methods in Engineering 79(11), pp. 1309-1331, 2009.

[34] M. S. Alnaes, J. Blechta, J. Hake, A. Johansson, B. Kehlet, A. Logg, C. Richardson, J. Ring, M. E. Rognes and G. N. Wells. *The FEniCS Project Version 1.5, Archive of Numerical Software 3* (2015). [doi.org/10.11588/ans.2015.100.20553]

[35] A. Logg, K.-A. Mardal, G. N. Wells et al. *Automated Solution of Differential Equations by the Finite Element Method*, Springer(2012). [doi.org/10.1007/978-3-642-23099-8]

[36] A. Logg and G. N. Wells. *DOLFIN: Automated Finite Element Computing*, ACM Transactions on Mathematical Software 37 (2010).

[37] A. Logg, G. N. Wells and J. Hake. *DOLFIN: a C++/Python Finite Element Library*, in: A. Logg, K.-A. Mardal and G. N. Wells (eds) Automated Solution of Differential Equations by the Finite Element Method (chapter 10), volume 84 of Lecture Notes in Computational Science and Engineering, Springer (2012).

[38] Matsumoto, M.; Nishimura, T. (1998). *"Mersenne twister: a 623-dimensionally equidistributed uniform pseudo-random number generator"* (PDF). ACM Transactions on Modeling and Computer Simulation.

8 Python3 code

Bellow is presented an indicative code for generating the results in Chapter (4.4). This is, by no way, a user friendly code, it's displayed only for more information about the commands used in the FEniCS environment and for result replication with different methods of approximation. Additionally, a generated *.msh* file is needed, in the folder file as the code, for representing the mesh.

```
from __future__ import print_function
from fenics import *
from mshr import *
import sys
import math
import meshio
import numpy as np


geo="Sphere"
NN=20 # MC iterations



geomesh= geo +".msh"
geoxd= geo + ".xdmf"
geopvd=geo +".pvd"


msh = meshio.read(geomesh)

tetra_cells = []
for cell in msh.cells:
    if cell.type == "tetra":
        if len(tetra_cells) == 0:
            tetra_cells = cell.data
        else:
            tetra_cells = vstack([tetra_cells, cell.data])

tetra_mesh = meshio.Mesh(points=msh.points, cells={"tetra": tetra_cells})
meshio.write(geoxd, tetra_mesh)


mesh = Mesh()
with XDMFFile(geoxd) as infile:
    infile.read(mesh)

    vtkfile = File('MESH/mesh_.pvd')
```

```
vtkfile << mesh


V=FunctionSpace(mesh, 'P', 1)

boundary_mesh = BoundaryMesh(mesh, 'exterior')
boundary_nodes = boundary_mesh.coordinates()
all_nodes = mesh.coordinates()
print('Boundary Mesh Nodes=',len(boundary_nodes))

print('Mesh Nodes=',len(all_nodes))


#sys.exit(" <Mesh> End")

########### Monte Carlo integral - BCs


integral=[]
count=[]

M=2 # alpha spale

mu=1.25663706*10**(-6)
r0=0.5

print('MC iterations per integral=',NN)



def BC(x,y,z):


  s=0.0
  v=0.0
  s1=0.0
  s2=0.0
  s3=0.0



  r=np.random.uniform(0,r0,NN)
  fi=np.random.uniform(0,np.pi,NN)
  theta=np.random.uniform(0,2*np.pi,NN)

  def diff_volume(r,theta,phi):
```

```
  return((np.sqrt(2)*(np.sin(phi)*np.cos(phi))*np.exp(-(1/float(M*r**2))))/fl
 for i in range(NN):

  v += diff_volume(r[i],theta[i],fi[i])
 v = v*((4/3)*np.pi*r0**3)/float(NN)


 s=v+s1+s2+s3

 return(s)


def F(x,y,z):
 return(-((np.sqrt(2)*z)/float(M*((x**2+y**2+z**2)**2)))*np.exp(-1/float(M*(x


def Mx(x,y,z):
    r=x**2 +y**2 +z**2
    theta=math.atan2(y,x)
    if(r<r0):
     s=-(np.sin(theta))*(np.sqrt(2)/2)*(math.exp((-1/(M*r**2))))
    else: s=0
    return(s)


def My(x,y,z):
    r=x**2 +y**2 +z**2
    theta=math.atan2(y,x)
    if(r<r0):
     s=(np.cos(theta))*(np.sqrt(2)/2)*(math.exp((-1/(M*r**2))))
    else: s=0
    return(s)

def Mz(x,y,z):
    r=x**2 +y**2 +z**2
    if(r<r0):
     s=(np.sqrt(2)/2)*(math.exp((-1/(M*r**2))))
    else: s=0
    return(s)



def boundary(x, on_boundary):
    return on_boundary
```

```
class MyExpression0(UserExpression):
    def eval(self, value, x):
        value[0]= BC(x[0],x[1],x[2])
    def value_shape(self):
        return ()


class MyExpression1(UserExpression):
    def eval(self, value, x):
        value[0]= F(x[0],x[1],x[2])
    def value_shape(self):
        return ()



class MyExpressionMx(UserExpression):
    def eval(self, value, x):
        value[0]= Mx(x[0],x[1],x[2])
    def value_shape(self):
        return ()

class MyExpressionMy(UserExpression):
    def eval(self, value, x):
        value[0]= My(x[0],x[1],x[2])
    def value_shape(self):
        return ()

class MyExpressionMz(UserExpression):
    def eval(self, value, x):
        value[0]= Mz(x[0],x[1],x[2])
    def value_shape(self):
        return ()


M_x=MyExpressionMx()
M_y=MyExpressionMy()
M_z=MyExpressionMz()


u_D = MyExpression0()
bc = DirichletBC(V, u_D, boundary)


# Define variational problem
u = TrialFunction(V)
v = TestFunction(V)
```

```
f = MyExpression1()
a = dot(grad(u), grad(v))*dx
L = f*v*dx

# Compute solution
Phi = Function(V)

solve(a == L, Phi, bc)


####Plot
vtkfile_B = File('solution/phi.pvd')
vtkfile_B <<Phi

V_vec = VectorFunctionSpace(mesh, "CG", 1)
H = project(grad(Phi), V_vec)
Mag1=project(as_vector((M_x,M_y,M_z)),V_vec)

B=project(mu*(H +Mag1),V_vec)


vtkfile_B = File('solution/B_tot.pvd')
vtkfile_B << B

vtkfile_B = File('solution/Mag1.pvd')
vtkfile_B << Mag1

vtkfile_B = File('solution/H.pvd')
vtkfile_B << H


source= Sphere(Point(0.0, 0.0, 0.0), r0, segments=24)
mesh_source=generate_mesh(source,42)

vtkfile_B = File('MESH/source.pvd')
vtkfile_B << mesh_source

sys.exit("<Solution>End")
```